



HAL
open science

A method for improving hotspot directional signatures in BRDF models used for MODIS

Ziti Jiao, Crystal B. Schaaf, Yadong Dong, Miguel Román, Michael J. Hill,
Jing M. Chen, Zhuosen Wang, Hu Zhang, Edward Saenz, Rajesh Poudyal, et
al.

► **To cite this version:**

Ziti Jiao, Crystal B. Schaaf, Yadong Dong, Miguel Román, Michael J. Hill, et al.. A method for improving hotspot directional signatures in BRDF models used for MODIS. *Remote Sensing of Environment*, 2016, 186, pp.135 - 151. 10.1016/j.rse.2016.08.007 . hal-01587526

HAL Id: hal-01587526

<https://hal.science/hal-01587526v1>

Submitted on 20 Aug 2021

HAL is a multi-disciplinary open access archive for the deposit and dissemination of scientific research documents, whether they are published or not. The documents may come from teaching and research institutions in France or abroad, or from public or private research centers.

L'archive ouverte pluridisciplinaire **HAL**, est destinée au dépôt et à la diffusion de documents scientifiques de niveau recherche, publiés ou non, émanant des établissements d'enseignement et de recherche français ou étrangers, des laboratoires publics ou privés.

1 A method for improving hotspot directional signatures in BRDF models used for

2 MODIS

3
4 Ziti Jiao^{1,2,*}, Crystal B. Schaaf^{3,4}, Yadong Dong^{1,2}, Miguel Román⁵,

5 Michael J. Hill⁶, Jing M. Chen⁷, Zhuosen Wang^{3,4,5}, Hu Zhang^{1,2}, Edward Saenz³,

6 Rajesh Poudyal⁸, Charles Gatebe⁹, Francois-Marie Bréon¹⁰, Xiaowen Li^{1,2}, Alan Strahler⁴

7
8 ¹ State Key Laboratory of Remote Sensing Science, Research Center for Remote Sensing and GIS, and School of
9 Geography, Beijing Normal University. Beijing 100875, China;

10 ² Beijing Key Laboratory of Environmental Remote Sensing and Digital City, Beijing Normal University, Beijing 100875,
11 China

12 ³ Department of Environmental, Earth and Ocean Sciences, University of Massachusetts, Boston, MA, USA

13 ⁴ Center for Remote Sensing, Department of Earth and Environment, Boston University, Boston, MA, USA

14 ⁵ Terrestrial Information Systems Laboratory, NASA Goddard Space Flight Center, Greenbelt, MD, USA

15 ⁶ Department of Earth System Science and Policy, University of North Dakota, Clifford hall, 4149 University Avenue,
16 Grand Forks, ND, 58202

17 ⁷ Department of Geography and Program in Planning, University of Toronto, 100 St. George St., Room 5047, Toronto,
18 Ontario, Canada M5S 3G3

19 ⁸ Science Systems & Applications, Inc., NASA Goddard Space Flight Center, Lanham, MD, USA

20 ⁹ Universities Space Research Association, NASA Goddard Space Flight Center, Greenbelt, Maryland, USA

21 ¹⁰ Laboratoire des Sciences du Climat et de l'Environnement, CEA/DSM/LSCE, 91191 Gif sur Yvette, France

22 *email: jiaozt@bnu.edu.cn

23

24

25 **Abstract:**

26 The semi-empirical, kernel-driven, linear RossThick-LiSparseReciprocal (RTLSR) Bidirectional
27 Reflectance Distribution Function (BRDF) model is used to generate the routine MODIS
28 BRDF/Albedo product due to its global applicability and the underlying physics. A challenge of
29 this model in regard to surface reflectance anisotropy effects comes from its underestimation of
30 the directional reflectance signatures near the Sun illumination direction; also known as the
31 hotspot effect. In this study, a method has been developed for improving the ability of the
32 RTLSR model to simulate the magnitude and width of the hotspot effect. The method corrects
33 the volumetric scattering component of the RTLSR model using an exponential approximation of
34 a physical hotspot kernel, which recreates the hotspot magnitude and width using two free
35 parameters (C_1 and C_2 , respectively). The approach allows one to reconstruct, with reasonable
36 accuracy, the hotspot effect by adjusting or using the prior values of these two hotspot variables.
37 Our results demonstrate that: (1) significant improvements can be made to this method by using
38 the inverted hotspot parameters; (2) the reciprocal nature allow this method to be more adaptive
39 for simulating the hotspot height and width with high accuracy, especially in cases where hotspot
40 signatures are available; and (3) while the new approach is consistent with the heritage RTLSR
41 model inversion used to estimate intrinsic narrowband and broadband albedos, it presents some
42 differences for vegetation clumping index (CI) retrievals. With the hotspot-related model
43 parameters determined *a priori*, this method offers improved performance for various ecological
44 remote sensing applications; including the estimation of canopy structure parameters.

45 Keywords: BRDF, CAR, MODIS, POLDER, multiangle remote sensing, hotspot signature,
46 hotspot kernel, linear RTLSR model, airborne measurements
47

48 **1. Introduction**

49 Semi-empirical kernel-driven linear Bidirectional Reflectance Distribution Function (BRDF)
50 models have been widely used to determine the properties of complex heterogeneous
51 environments from multi-angle remote sensing. These models have been used to produce the
52 routine BRDF/Albedo products from the Moderate Resolution Imaging Spectroradiometer
53 (MODIS) (Lucht et al., 2000; Schaaf et al., 2002; Schaaf et al., 2011), the Polarization and
54 Directionality of the Earth's Reflectances (POLDER) (Bicheron and Leroy, 2000; Bacour and
55 Bréon, 2005), the Meteosat Second Generation (MSG) (van Leeuwen and Roujean, 2002; Geiger
56 et al., 2005), and the Visible/Infrared Imager/Radiometer Suite (VIIRS) on board the platforms
57 of the Suomi National Polar-orbiting Partnership (NPP) (Justice et al., 2013). They have been
58 also used to retrieve canopy structure parameters (e.g., Chopping et al., 2008; Wang et al., 2011;
59 Hill et al., 2011; He et al., 2012), to examine the improved accuracy of land cover classification
60 (de Colstoun et al., 2006; Jiao, Woodcock & Schaaf et al, 2011; Jiao & Li, 2012), to accumulate
61 and apply prior knowledge of BRDF archetypal shapes (Li, Gao, Wang & Strahler, 2001; Jiao,
62 Hill, Schaaf et al., 2014; Jiao, Zhang & Dong et al., 2015), to couple surface reflectance with
63 atmospheric scattering for improving atmospheric correction algorithms (Hu et al., 1999; Wang
64 et al., 2010; Román et al., 2010; Litvinov et al., 2011), to correct for the effect of
65 remotely-sensed anisotropic reflectance (e.g., Leroy and Roujean, 1994; Li et al., 1996), and for
66 monitoring ecosystem disturbance and vegetation dynamics (e.g., Friedl et al., 2002, 2010;
67 Zhang et al., 2003).

68 Despite their wide use, recent studies have recognized that the directional signatures near

69 the Sun illumination direction (aka the hotspot effect) are often underestimated by the
70 semi-empirical BRDF models (e.g., Chen and Cihlar, 1997; Maignan et al., 2004; Román et al.,
71 2011) such as RTLSR (Wanner et al., 1995; Lucht et al., 2000). In particular, the volumetric
72 scattering (aka Ross) component of RTLSR, originally derived from a horizontally homogeneous
73 plant canopy (Ross, 1981), does not include all possible correlations between the illumination
74 and observation geometries (Kuusk, 1991; Jupp and Strahler, 1991; Qin & Geol, 1995). Although
75 the geometric-optical (Li-Strahler) component derived from geometric optical (GO) models
76 characterizes a significant hotspot effect (Li and Strahler, 1992), the RTLSR model that linearly
77 combines these two (Ross and Li-Strahler) components has difficulties to simulate the both the
78 magnitude and signature of the hotspot effect. This model deficiency, while not significantly
79 impacting an albedo retrieval (Huang, Jiao & Dong et al., 2013) (based on the integral of the
80 entire view-illumination hemisphere), may still constrain the application of BRDF models in
81 retrieving canopy structure parameters (e.g., clumping index) that need the hotspot amplitude as
82 primary input (e.g., He et al., 2012; Zhu et al., 2012).

83 Various efforts have been made to improve the hotspot effect for such models. Chen and
84 Cihlar (1997) enhanced the hotspot effect of the kernel-driven Roujean BRDF model by
85 multiplying the model with an exponential approximation of a physically-based hotspot function.
86 He et al. (2012) and Zhu et al. (2012) suggested that the Chen and Cihlar (1997) model might
87 still slightly underestimate the reflectance magnitude when it is used to extrapolate the hotspot.
88 Recent efforts have focused on correcting the RossThick kernel with a hotspot factor (Maignan
89 & Bréon et al., 2004; hereafter referred to as the Maignan method) based on the geometrical

90 principles of the intersection of viewed and sunlit leaf areas (Jupp and Strahler, 1991). With a
91 view to improving retrieval of clumping index (CI) from the MODIS BRDF product, He et al.
92 (2012) also developed a correction for the MODIS hotspot amplitude by adding the difference
93 between POLDER and MODIS hotspot BRFs, which has also been used to correct the hotspot
94 magnitude of MISR BRFs for CI retrievals (Pisek, Ryu, Sprintsin & He et al., 2013). On the
95 other hand, Zhu et al. (2012) corrected the hotspot amplitude by multiplying both the geometric
96 optical scattering and volumetric scattering items by the exponential approximation of a
97 modified hotspot function; also based on the MODIS RTLSR model.

98 In this study, we propose a method for improving the hotspot effect of the linear RTLSR
99 BRDF model. The method revises the RossThick kernel using the corrected exponential
100 approximation of the hotspot function (Chen and Cihlar, 1997, thereafter named RTCLS model
101 here). The principle of the formation of the hotspot is based on a canopy gap size distribution
102 function, but is approximated by using an exponential function with two free parameters (C_1 and
103 C_2) characterizing the height and width of the hotspot effect. The hotspot kernel within-crown
104 and between-crown has very similar shapes, and thus can be directly applied to the scenario
105 where a canopy cover is provided with a uniform leaf orientation of horizontally homogeneous
106 plant canopies, as was used in the assumption in deriving this kernel from canopy radiative
107 transfer theory (Ross, 1981). Such a correction to the RossThick kernel mainly accounts for the
108 correlation between two gap probabilities from sun and view in the hotspot direction, which was
109 not properly considered when deriving the original RossThick kernel.

110 To validate this model, the study uses a variety of hotspot data to determine appropriate

111 hotspot-related parameters including POLDER, MODIS, airborne multiangle Cloud Absorption
112 Radiometer (CAR) (King et al., 1986, Gatebe et al., 2003, Román et al., 2011), and two
113 field-measured data sets (Irons et al., 1992; Deering et al., 1999). We also explore the sensitivity
114 of two hotspot parameters (C_1 and C_2) to hotspot-fits. Finally, we examined the influences of this
115 new approach on the retrieval of intrinsic albedos and clumping index.

116 **2. Hotspot data**

117 **2.1. POLDER-3 BRDF database**

118 The spaceborne POLDER instrument can sample the land surface for viewing angles up to
119 60° - 70° and for the full azimuth range, at a coarse spatial resolution of approximately 6 km.
120 Comprehensive BRDF sampling with large spatial coverage enables this instrument to collect
121 observations for the development of BRDF modeling, particularly capturing distinct hotspot
122 signatures. The POLDER-3 sensor onboard the Polarization and Anisotropy of Reflectances for
123 Atmospheric Sciences coupled with Observations from a Lidar (PARASOL) satellite acquired
124 multiangular measurements for more than 6 years, which were used to create four BRDF
125 databases (Bréon et al., 2007). The approach uses POLDER data from relatively homogeneous
126 pixels to represent the dominant continental ecosystems. The data are geocoded, calibrated,
127 atmospherically-corrected and cloudy-screened for acquiring the land surface bidirectional
128 reflectance factors (BRFs) for each orbit. This study uses a monthly database containing 14,649
129 BRFs in 16 IGBP land cover classes. According to phase angle $\xi \leq 5^\circ$, we extract $\sim 14,188$ BRFs.
130 The spatial distribution of view and Sun geometries for a typical POLDER data set, i.e.,
131 IGBP_01_20060609brdf_ndvi08.0824_1671, is exemplified in Figure 1 (b). Since the ‘Snow and

132 Ice' class tends to have maximum reflectance in forward scattering direction that current surface
133 BRDF models cannot characterize, we exclude this class from the database. The BRDF signatures
134 are based on inversions of approximately 20 orbits worth of spectral BRDF data, for each of the
135 six POLDER bands. Up to 16 different multiangular measurements for a given POLDER pixel
136 are included in each orbit. BRDFs measured at two typical bands (red, centered 670 nm and NIR,
137 centered 865 nm) are mainly selected to assess the hotspot effect reconstructed from the
138 proposed model. Notably, POLDER-3 spectral measurements are not simultaneous, meaning that
139 each channel is acquired with a slightly different viewing geometry. As such, to analyze the
140 variability of hotspot signatures, this requires a careful assessment of measurement differences,
141 including normalization of the POLDER viewing geometry (Bréon et al., 2005).

142 **2.2. MODIS hotspot data**

143 We extracted 2,275 MODIS hotspot data sets from one $10^\circ \times 10^\circ$ tile (h20v11) of MODIS
144 surface reflectance products (MOD09 and MYD09) at a spatial resolution of approximately
145 500-m, for 7 solar reflective bands, and using high-quality BRDF sampling distributions,
146 represented by a phase angle range $\xi \leq 5^\circ$. There are only 80 high-quality hotspot data sets within
147 a phase angle range of $\xi \leq 1.5^\circ$; indicating that MODIS seldom acquires exact hotspot
148 observations. Each data set consists of at least 10 observations with a proper directional sampling
149 in approximate principal plane (PP), and includes fewer hotspot measurements within the
150 defined area (Figure 1, a). The corresponding MODIS tile h20v11 captures a wide range of
151 grass-shrub-savanna vegetation types in the Southern Hemisphere. The 329th Day of Year (DOY)
152 in 2010 represents a maturity season (Zhang et al., 2003). Solar zenith angles (SZAs) mainly

153 ranged from 20° to 40° during the study period. The full-model inversion quality of the MODIS
154 BRDF/Albedo product (MCD43A2) accounts for approximately 70 % of total pixels. The spatial
155 distribution of MODIS observations and solar geometry from an extreme data set in this tile is
156 presented in Figure 1 (c), where solid points are for MODIS observations, and circles are for
157 solar geometries. The concentric circles are at 20° intervals.

158 Since the Terra and Aqua MODIS accumulate multiangular observations through multiple
159 overlapping image swaths, the solar geometry corresponding to each observation will be
160 different during a typical (16-day) retrieval period (e.g., approximately 20° for SZA in the
161 h20v11 tile). This means that MODIS does not capture enough real-time observations in the
162 principal plane (PP) under identical solar illumination conditions. Here, we adopt the assumption
163 used with the MODIS BRDF/Albedo product, whereby the surface BRDF shape doesn't change
164 abruptly for the range of SZAs capturing during a 16-day retrieval period. With this assumption,
165 we can accumulate some multiangular observations in the proximity of the hotspot (i.e., $\xi \leq 5^\circ$)
166 to constrain the RTCLSR model for acquiring the optimal free parameters describing the hotspot
167 magnitude (C_1) and width (C_2). Figure 1 (d) presents an extreme example that uses the RTCLSR
168 model to reconstruct BRDF shapes as a function of phase angle for IGBP savanna in the NIR
169 band. Red solid points represent observations extracted by using this method in the approximate
170 PP. The black curve is the reconstructed BRDF shape using the RTCLSR model with $C_1=0.4$,
171 and $C_2=4.5^\circ$ as the optimal values for the 2,275 MODIS data sets in this tile. The SZA was set to
172 30.58° , and the observation in the closest proximity to the hotspot direction is 31° (red point).

173 The BRDF shape reconstructed using the Maignan method (green curve) is provided here for
174 visual comparison.

175 Figure 1 near here

176 **2.3. Finer resolution measurements**

177 We used airborne datasets collected by NASA's Cloud Absorption Radiometer (CAR)
178 (Gatebe et al., 2003), which captures hotspot signatures over 2 field sites. To acquire
179 multiangular measurements, the CAR instrument is flown using a clockwise circular pattern
180 above the surface repeatedly, and observes the reflected solar radiation at a fine angular
181 resolution (i.e., 0.5° intervals through its 190° aperture at a rate of 100 scans per minute). This
182 sampling scheme results in a BRDF retrieval that is based on 76,400 and 114,600 BRFs
183 measurements per channel per complete orbit, which corresponds to a representative sample of
184 the landscape-level (~ 5 km) reflected surface (Gatebe et al., 2003). At an altitude of 600m above
185 the targeted surface area and 1° instantaneous field of view (IFOV), the pixel resolution is about
186 10 m at nadir and about 270 m at an 80° viewing angle (Tsay et a., 1998). The geolocation
187 accuracy of CAR measurements is within an error margin of 0.3% (~ 2.0 - 3.5 meters as derived
188 from the high resolution scene across the entire scan track). This accuracy holds well particularly
189 with off-nadir looking observations (Gatebe et al., 2007). These CAR measurements used in this
190 study are averaged at an angular resolution of 1° in the viewing hemisphere and are taken in the
191 red ($0.682 \mu\text{m}$) and NIR ($0.870 \mu\text{m}$) bands.

192 CAR data source was mainly from the early Smoke Clouds and Radiation-Brazil (SCAR-B)
193 field campaign on August, 1995. Two kinds of data sets were collected from the well-defined

194 surfaces of cerrado and dense forest (Tsay et al., 1998), both measured in Brazil under nearly
195 clear-sky conditions (http://car.gsfc.nasa.gov/data/index.php?mis_id=5&n=SCAR-B&l=h). The
196 cerrado comprises a landscape-scale mosaic of four main vegetation types ranging from *campo*
197 *limpo* grassland, through *campo sujo* and *campo ralo* with small (< 2m) sparse-to-medium
198 density woody plants overlaying grassland, to *cerrado sensu stricto* with 20 – 30 t/ha of woody
199 biomass. The dense forest data includes two flight data (i.e., CAR Flight #1689 and CAR Flight
200 #1693). These two forest data captured distinct hotspot signatures in the red (CAR Flight #1689)
201 and the NIR (CAR Flight #1693) bands, and are used in this study. The area of dense forest was
202 covered by tall trees with a large canopy where the ground surface is invisible and had a
203 relatively homogeneous surface. Details about these airborne CAR measurements are referred to
204 Tsay et al. (1998).

205 To compare these models being explored at a field scale, we also analyzed two high-quality
206 multiangular field data sets reported in previous studies (e.g. Li et al., 2001; Strugnell et al., 2001;
207 Huang & Jiao 2012; Jiao et al., 2014). These include soil multiangular measurements (Iron et al.,
208 1992) acquired on a bare field located on a level alluvial plane within the United States
209 Department of Agriculture Beltsville Agricultural Research Center, Beltsville, MD. The data
210 were taken from full view angles and several solar illumination directions. A calibrated Barnes
211 Model 12-1000 Modular Multiband Radiometer (MMR) with a 15° IFOV was used. Forest
212 multiangular measurements (Deering et al., 1999) were also acquired with PARABOLA
213 instrument with a 15° IFOV at a black spruce site that was mainly made up of old black spruce
214 (*picea mariana*) with scattered emergent tamarack. The tree height was less than 10 m and the

215 total stem density was 8040 live stems/ha, with a basal area of 40 m²/ha. Canopy closure
 216 averaged about 55 %, and the leaf area index (LAI) measured by an LAI-2000 in spring 1994
 217 was 3.7 (Chen et al., 1997).

218 **3. Model and method**

219 **3.1. RTLSR model**

220 The semi-empirical, kernel-driven, linear BRDF model is a linear combination of three
 221 basic scattering components: isotropic scattering, volumetric scattering, and geometric-optical
 222 (GO) scattering. This model adopted a general form (Roujean et al., 1992; Lucht et al., 2000):

$$223 \quad R(\theta_v, \theta_s, \Delta\phi, \lambda) = f_{iso}(\lambda) + f_{vol}(\lambda)K_{vol}(\theta_v, \theta_s, \Delta\phi) + f_{geo}(\lambda)K_{geo}(\theta_v, \theta_s, \Delta\phi) \quad (1)$$

224 Where $f_{iso}(\lambda)$, $f_{vol}(\lambda)$ and $f_{geo}(\lambda)$ are the spectrally dependent model parameters. $K_{vol}(\theta_v, \theta_s, \Delta\phi)$ and
 225 $K_{geo}(\theta_v, \theta_s, \Delta\phi)$ are kernel functions of view zenith θ_v , illumination zenith θ_s and relative azimuth
 226 $\Delta\phi$ and provide shapes for volumetric scattering and geometric-optical scattering BRDFs; $f_{iso}(\lambda)$
 227 is a spectral constant for isotropic scattering; $f_{vol}(\lambda)$ and $f_{geo}(\lambda)$ are spectral constants, i.e., model
 228 anisotropic parameters that weight the two BRDFs; $R(\theta_v, \theta_s, \Delta\phi, \lambda)$ is BRDF in waveband λ .

229 K_{geo} and K_{vol} have been derived from physical approximation of the radiative transfer at the
 230 surface. K_{geo} is derived from the GO model (Li and Strahler, 1992; Roujean et al., 1992) and
 231 characterizes dome-shaped BRDF curves. It is a function that describes the shadowing and
 232 surface scattering from the canopy. The operational MODIS BRDF/Albedo algorithm adopted
 233 the LiSparseReciprocal kernel (K_{LSR}) that was derived from a sparsely-vegetated canopy surface.

$$234 \quad K_{LSR} = O(\theta_v, \theta_s, \Delta\phi) - \sec\theta'_v - \sec\theta'_s + \frac{1}{2}(1 + \cos\xi')\sec\theta'_v \sec\theta'_s \quad (2)$$

235 Notably, where $O(\theta_v, \theta_s, \Delta\phi)$ is overlap function of view and illumination shadows on the ground,

236 and hence the hotspot effect (i.e., the probability of seeing the sunlit background from the same
 237 gap) is included in this kernel. Further expressions and several intermediate variables are detailed
 238 to several papers (e.g., Wanner et al., 1995; Lucht et al., 2000).

239 Notably, two ratios (h/b and b/r) for describing vegetation structure are used to parameterize
 240 overlap function in K_{LSR} . Here, h is the mean height where a crown center is located, b is the
 241 mean vertical half axis of the modeled ellipsoid, and r is the mean horizontal radius. These two
 242 ratios are related to the hotspot effects in K_{LSR} on vegetation canopy scale (Li and Strahler, 1992).
 243 The operational MODIS RTLSR algorithm adopts $h/b=2$ and $b/r=1$. In Figure 2 (top), red dashed
 244 curve is for $h/b=2$ and $b/r=1.2$, and magenta dashed curve is for $h/b=2.5$ and $b/r=1$. Figure 2
 245 demonstrates that, although these two ratios were in theory related to the general hotspot effect in
 246 K_{LSR} , they do not seem to be very sensitive to the changes of hotspot effect at a reasonable range.

247 K_{vol} is a similar function that describes the volumetric scattering component from canopy,
 248 based on an assumption of a single-scattering approximation of the radiative transfer (RT) theory
 249 by Ross (1981). The operational RTLSR model adopted RossThick kernel (K_{RT}) derived from a
 250 homogenously layered canopy with a large leaf area index (LAI) (Wanner et al., 1995)

$$251 \quad K_{RT} = \frac{\left(\frac{\pi}{2} - \xi\right) \cos \xi + \sin \xi}{\cos \theta_v + \cos \theta_s} - \frac{\pi}{4} \quad (3)$$

252 This kernel characterizes bowl-shaped BRDF curves, but does not consider the correlation
 253 between illumination and observation processes for the observed hotspot. In theory, the
 254 probability of observing a sunlit component can be taken as the product of two probabilities: one

255 for the view line from the observer and the other for illumination beam from Sun. When the view
 256 line and an illumination beam coincide, the observer either sees the sunlit foliage or the sunlit
 257 background, while the shadows of foliage and background are hidden from the view. As a result,
 258 the correlation tends to be 1:1, as the illumination and view directions get closer.

259 **3.2. RTLSR hotspot correction**

260 To consider the correlation between the view and illumination processes, Maignan et al.
 261 (2004) corrected the K_{RT} with a hotspot factor:

$$262 \quad K_{RTM} = \frac{\left(\frac{\pi}{2} - \xi\right) \cos \xi + \sin \xi}{\cos \theta_v + \cos \theta_s} \times \left(1 + \left(1 + \xi / \xi_0\right)^{-1}\right) - \frac{\pi}{4} \quad (4)$$

263 $1 + \left(1 + \xi / \xi_0\right)^{-1}$ is a simplified hotspot factor derived by Bréon et al. (2002) from the theory on
 264 the calculation of an overlay function of the intersection of viewed and sunlit leaf areas (Jupp &
 265 Strahler, 1991). This hotspot factor was used to correct K_{RT} , thereafter named K_{RTM} . Here ξ is
 266 phase angle, ξ_0 is a characteristic angle in relation to the ratio of scattering element size and the
 267 canopy vertical density, which follows the range $\xi_0 = [1^\circ, 2^\circ]$. A $\xi_0 = 1.5^\circ$ has been suggested as a
 268 typical value representing a wide range of landscape conditions (Bréon et al., 2002; Maignan et
 269 al., 2004).

270 Note that the K_{RTM} value near the hotspot direction will double rapidly (as much as K_{RT}) as
 271 the phase angle ξ approaches 0° . To consider hotspot variability, we specified a $\xi_0 = 3.0^\circ$ for
 272 K_{RTM} for a comparison with the standard $\xi_0 = 1.5^\circ$ (Figure 2). The results indicate that an increase
 273 in ξ_0 can increase hotspot width, but diverge from K_{RT} beyond the hotspot region compared

274 with K_{RTC} . Therefore, we do not further examine the ξ_0 influence on hotspot-fits in this study,
 275 rather than adopt $\xi_0=1.5^\circ$ as the most appropriate value. Here, the K_{RTM} has a simplified feature
 276 whereby the variation in hotspot height and width is determined by phase angle ζ .

277 For volumetric scattering kernel (K_{vol}), it is frequently required to meet the empirical
 278 requirement of $K_{vol} = 0$ when both the viewing and illumination geometries point to nadir. This
 279 requirement aims to ensure that the isotropic parameter is physically reflectance for the model
 280 retrieval (Roujean et al., 1992). Conversely, using the Maignan method, the nadir-view and
 281 nadir-sun reflectance are specified as $R(0,0,0,\lambda) = f_{iso}(\lambda) + f_{vol}(\lambda) \times \pi/4$.

282 Here, we introduce the modified exponential function of the hotspot kernel function to K_{RT} ,
 283 hereby termed the RossThickChen kernel (K_{RTC}), which includes two free parameters
 284 characterizing hotspot variations (Chen and Cihlar, 1997):

$$285 \quad K_{RTC} = \frac{\left(\frac{\pi}{2} - \xi\right) \cos \xi + \sin \xi}{\cos \theta_v + \cos \theta_s} \times \left(1 + C_1 e^{-\frac{\xi}{C_2}}\right) - \frac{\pi}{2} \quad (5)$$

286 Where $1 + C_1 e^{-\frac{\xi}{C_2}}$ is the modified hotspot function. The two free parameters, C_1 and C_2 , allow a
 287 large dynamic range of hotspot variation, and thus facilitate the analysis of the variation of
 288 hotspot height and width in fitting hotspot BRDFs. For this retrieval, we also make an empirical
 289 adjustment to retain the isotropic BRDF model parameter, f_{iso} , as the corresponding nadir-view
 290 and nadir-sun BRDF.

291 Originally, the K_{RTC} hotspot function was derived from a theoretical expression that
 292 accounts for the hotspot effect for a forest stand, based on a geometric-optical model (Chen &
 293 Leblanc, 1997). In this specific scenario, C_1 , is linearly related to the difference between the

294 reflectances of the foliage and background at the wavelengths of interest (Chen & Cihlar, 1997).
295 In deriving this hotspot kernel, Chen and Leblanc (1997) demonstrated that this modification had
296 very similar shapes at within-crown and between-crown scales because the gap size is scaled by
297 the gap depth. For plane parallel layers of leaves, the average gap depth is taken as the mean
298 distance between two layers of leaves and is related to the leaf area density. In this hotspot
299 function (K_{RTC}), C_1 is related to the magnitude of the hotspot peak, while C_2 defines the half
300 width of the hotspot in relation to the ratio of canopy height to the size of the predominant
301 canopy structure. Notably for this study, to keep consistent with the original kernel form, the unit
302 of C_2 is radians in terms of Eq. (5), but it is converted into degrees in subsequent use to describe
303 the hotspot width.

304 Here, the K_{RTC} kernel is empirically adjusted to meet $K_{RTC} = 0$ for the nadir-view and
305 nadir-sun geometries, which results in a downward shift of kernel shape (Figure 2, bottom). Note
306 that this adjustment does not affect the fitting ability of this model since the kernel shape is
307 retained. Figure 2 aligns K_{RTC} with K_{RT} and K_{RTM} for a convenient comparison. The results
308 indicate that K_{RTC} coincides with K_{RT} in the scattering direction beyond hotspot region, and
309 adjusts the hotspot height and width by changing C_1 and C_2 (Figure 2 bottom). A larger C_1 value
310 also indicates a higher hotspot, while a larger C_2 value indicates a wider hotspot.

311 Figure 2 near here

312 **3.3. Hotspot parameter retrieval and analysis**

313 The inversion strategy for retrieving the three parameters of this linear BRDF model is to
314 minimize the root mean square error (RMSE) between model predicted and observed BRFs. The

315 full-inversion is a simple matrix inversion that is independent of land surface types and is
 316 performed pixel by pixel using all high-quality measurements available. Details are referred to
 317 the papers (Roujean et al., 1992; Lucht et al., 2000; Shuai et al, 2008).

318 To derive the C_1 and C_2 values, we calculated fit-RMSEs to minimize the
 319 model-observation fits using accumulated measurements in a close vicinity to the hotspot
 320 direction (i.e., $\xi \leq 5^\circ$).

$$321 \quad RMSE = \sqrt{\frac{\sum_{j=1}^n (R^{obs}(\theta_v, \theta_s, \Delta\phi, \lambda) - R^{model}(\theta_v, \theta_s, \Delta\phi, \lambda))^2}{n-3}} \quad (6)$$

322 Where $R^{obs}(\theta_v, \theta_s, \Delta\phi, \lambda)$ and $R^{model}(\theta_v, \theta_s, \Delta\phi, \lambda)$ are the model predicted and observed BRFs near
 323 the hotspot region in the viewing and solar geometries, $\theta_v, \theta_s, \Delta\phi$ at wavelength λ , as in Equation
 324 (1). We derived the optimized C_1 and C_2 values from the least RMSEs using the iteration step
 325 size of 0.1 for $C_1 = [0.3, 1.2]$ and $C_2 = [1.0^\circ, 6.0^\circ]$. This range of C_1 and C_2 can ensure realistic
 326 hotspot variations while optimizing processing time. Following this method, we retrieved the C_1
 327 and C_2 values for the entire POLDER database; including parameterizations by IGBP cover type
 328 and phenological phase, respectively. To derive the optimal hotspot parameter values, we
 329 constrain this model by accumulating all measurements near hotspot direction ($\xi \leq 5^\circ$) for these
 330 two parameter types, including all 15 IGBP classes, excluding ‘Snow and Ice’ and 2 phenological
 331 stages: (1) maturity and (2) dormancy.

332 We then compared the model predicted and observed BRFs near hotspot direction by using
 333 scatterplots with regression lines. To display model-observation fits, we examined the model
 334 predicted and observed BRFs as a function of phase angle for the selected observations for

335 Evergreen Needleleaf Forest type (ENF) for each of POLDER's reflective bands. Details on how
336 to derive the shaded area (Figure 1, a) are provided in Appendix A. We also performed a
337 comparison against finer resolution in-situ data. To analyze the sensitivity of the hotspot
338 parameters to hotspot-fits in conjunction with the model parameters, we used simulated BRDF
339 shapes generated from the airborne CAR data set.

340 Finally, we examined the intrinsic albedos (i.e., White Sky Albedo (WSA) and Black Sky
341 Albedo (BSA)) and clumping index (CI) retrievals between models. To retrieve CI values, we
342 made use of the algorithm by Chen et al. (2005) and assigned a simplified geometry of 45° view
343 zenith angles in both the backward- and forward- scattering directions for the corresponding
344 principal plane hotspot and dark spot, respectively (Zhu et al. 2012). Such a simplification is
345 somewhat different from Chen et al. (2005), which focused on locating the optimal view
346 geometry to capture the dark spot. Since the three models are generally consistent in fitting
347 observations outside of the hotspot region, this simplification would not affect the
348 inter-comparison of CI retrievals between models.

349 **4. Results**

350 **4.1. C_1 and C_2 values for POLDER**

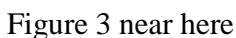
351 In this section, we assess the performance of the two hotspot parameters, based on the
352 underlying IGBP class and two vegetation phenological phases, based on a comparison of the
353 model predicted hotspot BRFs with observed BRFs derived from the POLDER BRDF database.
354 For this study, our analysis focuses on the RTCLSR and Maignan method.

355 **4.1.1. Hotspot parameters in regard to surface type and phenology**

356 Figure 3 (top left) presents the globally optimized C_1 and C_2 values (RTCLSR_GLOB) for 6
357 POLDER bands [490, 565, 670, 765, 865, and 1020nm]. These values indicate the variation
358 trend of hotspot parameters for the available POLDER BRDF database. In general, the spectral
359 variations of C_1 and C_2 present a highly negative correlation ($R^2 = 0.58$). This indicates that a
360 higher hotspot magnitude also tends to go with a narrower shaped hotspot, and vice versa. Figure
361 3 (middle) presents the optimized C_1 and C_2 values derived for underlying IGBP classes in the
362 red and NIR bands. Results indicate that the C_1 values in the red band are larger than in the NIR
363 for all IGBP classes; indicating that the hotspot height is relatively prominent in red band. This is
364 due to the higher-level chlorophyll absorption of vegetation foliage in the red band, which
365 strengthens the sunlit-shaded component contrast, and results in a more prominent reflectance
366 anisotropy. The C_1 values are significantly different between some IGBP classes; particularly in
367 the red, and exhibits a high correlation between the red and the NIR ($R^2 = 0.62$). This reveals that
368 a higher hotspot in the red band is frequently accompanied by a higher hotspot in the NIR band.
369 However, the C_2 parameter presents a low correlation between the two bands ($R^2 = 0.21$),
370 indicating that hotspot width is not band-dependent for these BRDF data.

371 Figure 3 (top right) shows the near-hotspot fit-RMSEs ($\zeta < 5^\circ$) between models in 6 bands.
372 Results indicate that the fit-RMSEs are lower in the visible than in NIR and shortwave infrared
373 (SWIR). As expected, the RTLSR model had the largest fit-RMSEs in the vicinity of hotspot
374 direction. We also derived globally optimized fit-RMSEs (RTCLSR_GLOB) for the entire
375 POLDER data and the IGBP-bounded fit-RMSEs (RTCLSR_IGBP). The absolute average

376 difference (AAD) of the fit-RMSEs (left ordinate) between Maignan and RTCLSR_IGBP models
377 was 0.0023 per band, while the relative average difference (RAD) of fit-RMSEs (right ordinate)
378 between these two models was ~20-30% in the blue, red and NIR bands [490, 670, 765nm]. This
379 reveals that the RTCLSR model with the two free parameters can provide further improved
380 hotspot-fits. Figure 3 (bottom) presents the fit-RMSEs for 15 IGBP classes between models in
381 the red and NIR bands. Some improvements occur for several IGBP classes using the RTCLSR.
382 The improvements seem more pronounced for forest than for herbaceous classes in the red band,
383 while the opposite appeared to be the case in the NIR band.

384  Figure 3 near here

385 To examine the phenological response of C_1 and C_2 values for surface type, we used
386 mid-high latitude ($23.5^\circ \leq \text{latitude} \leq 60^\circ$) POLDER data in terms of the timing of Jun-Jul-Aug
387 and Dec-Jan-Feb in Northern Hemisphere to represent maturity and dormancy seasons; using
388 opposite time periods in the Southern Hemisphere. The C_1 and C_2 values were then retrieved for
389 each IGBP class in the red and NIR bands. Figure 4 shows that vegetation cover tends to have
390 larger C_1 and C_2 values in maturity, but less C_1 and C_2 values in dormancy in the red band. In the
391 NIR band, vegetation cover mainly captures less C_1 but larger C_2 in maturity and larger C_1 but
392 less C_2 in dormancy. Interestingly, these hotspot parameter values indicate that vegetation cover
393 mainly captures a higher and wider hotspot in maturity, but a lower and narrower hotspot in
394 dormancy in the red band. In the NIR band, vegetation cover mainly captures a lower but wider
395 hotspot in maturity, and a higher and narrower hotspot in dormancy. Such hotspot behaviors
396 should result from the leaf-on and leaf-off status in combination with spectral multiple scattering

397 effects within vegetation canopy in red and NIR bands. This provides direct evidence on the
398 spectral variability of the hotspot effect with respect to vegetation phenology.

399 As a comparison, Figure 4 (lower left) presents the average NDVI as a function of IGBP
400 class in maturity and dormancy seasons. NDVI values are generally bigger in maturity than in
401 dormancy for most IGBP classes. This indicates that the selected IGBP classes for this
402 phenological analysis are mainly in a leaf-on and leaf-off stage, respectively. Notably, the NDVI
403 values are very close for few classes (e.g. Shrubland, Woody Savannas and Urban), likely due to
404 the lack of green foliage across classes. Figure 4 (lower right) presents the fit-RMSEs by the
405 RTCLSR model for maturity and dormancy seasons in the red and NIR bands. The fit-RMSEs
406 are chiefly higher in the NIR than in the red, but do not show significant differences between
407 these two seasons. This comparison reveals that NDVI alone doesn't distinctly capture this type
408 hotspot variation as was detailed by using two hotspot parameters.

409 Figure 4 near here

410 **4.1.2. Hotspot BRFs**

411 The scatterplots in Figure 5 (top panel) show the agreement between model-predicted and
412 observed hotspot BRFs in the red and NIR bands for the entire POLDER database. The
413 correlations between the two are very high ($R^2 > \sim 0.90$) in both the red and NIR bands. In the red
414 band, the Maignan method slightly underestimates the hotspot BRF; particularly at a range of
415 low reflectances (i.e., bias = -0.005 for BRFs < 0.1), but overestimates hotspot BRFs at a range
416 of high reflectances (i.e., bias = 0.011 for BRFs \geq 0.4). In the NIR band, the Maignan method
417 overestimates hotspot BRFs by 0.014 units at a range of BRFs \leq 0.3, and by 0.008 at range of

418 BRFs > 0.4 . These biases are slightly corrected by using the RTCLSR model. Although the
419 RTCLSR model with two free parameters fits the hotspot BRFs a little better than the Maignan
420 method, the differences between them in fitting observed BRFs in the close proximity of hotspot
421 direction (i.e., $\xi \leq 1.5^\circ$) were minor.

422 To further examine these two models in fitting hotspot BRFs as a function of surface type,
423 we selected four IGBP classes to reflect a forest, mixed, grass, and sparsely vegetated gradient
424 representing different canopy physiognomies and structures. In the red band, the Maignan
425 method tends to underestimate the hotspot BRFs by 0.014 units for the ‘Evergreen Needleleaf
426 Forest’ (ENF) class. The underestimation is reduced to 0.011 units for the ‘Woody Savannas’
427 (WSa) class, and the model fits well (underestimates by 0.003) for the ‘Grasslands’ (GrL) class;
428 but somewhat overestimates by 0.009 units for the ‘Barren or Sparsely Vegetated’ (BSV) class.
429 The relative average difference (RAD) between these two model reaches to 12% for ENF class.
430 These biases are generally corrected by using the RTCLSR model (Figure 5). In the NIR band,
431 the biases in reconstructing hotspot BRFs by Maignan method are -0.007 for ENF, 0.001 for
432 WSa, -0.017 for GrL, and 0.018 for BSV. These biases are reduced to the range from -0.001 to
433 -0.003 by using the RTCLSR model. This demonstrates that the RTCLSR model can provide
434 further improvement for hotspot-fits for a subset of IGBP classes.

435 Figure 5 near here

436 To qualitatively compare the Maignan and RTCLSR models, Figure 6 presents model
437 predicted and observed BRFs for the ENF class as a function of phase angle in the proximity of
438 the principal plane in 6 bands. We only use the observations falling within the shaded area in

439 Figure 1 (a) to approximate the principal plane. Data sources are marked on each subplot with a
440 $SZA=44.89^\circ$ recording the hotspot direction. The NDVI values can be directly derived from the
441 data sources. The optimized C_1 and C_2 values for the ENF class in the corresponding bands are
442 used for each data set. This figure shows that the Maignan method and the RTCLSR model
443 generally capture the hotspot signatures very well for these POLDER data; however, Maignan
444 method seems to overestimate the hotspot height and underestimate hotspot width in blue band,
445 but somewhat underestimate hotspot width in other bands for this dataset. The RTCLSR model
446 presents more flexibility for capturing the hotspot observations. This is one of the key features of
447 the RTCLSR model; i.e., its ability to leverage the reciprocal nature of anisotropic reflectances to
448 improve retrieval quality.

449 Figure 6 near here

450 **4.2. Hotspot parameter values for one tile of MODIS hotspot data**

451 We retrieve two hotspot parameter values using one tile of MODIS hotspot data (h20v11)
452 (Table 2). In general, C_1 values are larger in lower reflectance, which indicates relatively
453 prominent hotspot effects due to lack of multiple scatterings from vegetation cover, which shows
454 a consistent variation tendency with two hotspot parameter values for POLDER data. C_1 and C_2
455 values do not present significant differences between three major land cover types in this tile,
456 dominated by savannas. However, the optimized C_1 and C_2 values present some differences in
457 the corresponding bands between MODIS and POLDER, likely because MODIS hotspot data are
458 derived only from one tile. From Figure 1 (d), we can also see that the BRDF shapes
459 reconstructed using the Maignan (green curve) and RTCLSR models (black curve) in the NIR

460 band are very close except for the hotspot peak. The optimal $C_1=0.4$ for 2,275 MODIS data sets
461 in this tile characterizes a low hotspot height, compared with the Maignan method for this
462 extreme example. Note that the MODIS has difficulty in acquiring sufficient hotspot signatures
463 on a global scale. As such, analysis of potential scale inconsistencies between MODIS and
464 POLDER was not comprehensively performed using current hotspot data.

465 **4.3. Results with in-situ and airborne data**

466 We used airborne CAR SCAR-B cerrado and forest measurements (Tsay et al, 1998), as
467 well as two high-quality field BRDF data sets (Iron et al., 1992; Deering et al., 1999) to evaluate
468 the RTCLSR approach. Measurements are limited in the proximity of the principal plane, and
469 hotspot observations are selected for $\xi \leq 1.5^\circ$ according to our sampling design (Figure 1, a). The
470 CAR cerrado dataset was collected on a forest-grass vegetation system that is known for its
471 distinct hotspot signature in the red and NIR bands. Dense forest covered by tall trees with a
472 close canopy had two-flight measurements. For these data sets, we only make use of the band
473 where the hotspot signature was the most prominent.

474 Using CAR SCAR-B cerrado measurements, Figure 7 presents the model predicted and
475 observed BRFs in the red and NIR bands (not shown for the RTLSR model). We provide three
476 specific cases to identify the potential difference between these two methods. Figure 7 (a-b)
477 present the optimized C_1 and C_2 for the RTCLSR model for this specific data set. Figure 7 (c-d)
478 use the $C_1 = 1.0$ and $C_2 = 3^\circ$ as default values because K_{RTC} with the default C values captures a
479 very close kernel shape with K_{RTM} (Figure 2). Figure 7 (e-f) present two-model consistencies by
480 adjusting two hotspot parameters of the RTCLSR model to approach to Maignan predicted

481 shapes for this specific data set (observations not shown). This comparison shows that the
482 RTCLSR model with two free hotspot parameters can approach to Maignan method to a very
483 great degree. Using CAR SCAR-B forest measurements, we compared the difference between
484 the model-predicted and observed BRFs in the principal plane, and over the entire viewing
485 geometries between two models (Figure 8). The difference in reconstructing the hotspot BRFs
486 between these two models are distinctly exhibited over the entire viewing hemisphere. We
487 further performed the statistical analysis for these two CAR datasets for BRFs near the hotspot
488 region of phase angle $\xi \leq 5^\circ$ and within the viewing hemisphere of $VZA \leq 75^\circ$ (Figure 9). While
489 these two approaches do not present difference for the entire CAR datasets, the significant
490 improvement occurs in recreating hotspot signatures using the optimized hotspot parameters of
491 the RTCLSR model for the RMSEs, biases and correlation coefficients (Figure 9).

492 Figure 7, 8 and 9 near here

493 Finally, we compared the RTLSR, RTCLSR, and Maignan models fits to the field
494 measurements collected from soil and vegetation surface (Figure 10). A $C_1=0.4$ and a $C_2=5.2^\circ$ are
495 the optimal values for the soil measurements in the red, and $C_1=1.3$ ($C_2=10^\circ$) and $C_1=1.0$
496 ($C_2=8.0^\circ$) capture the best hotspot-fits for the black spruce (*picea mariana*) in the red and NIR
497 bands. Results indicate a significant difference between the model-predicted hotspot BRFs for
498 the soil and the black spruce surfaces. The RTCLSR model with a $C_1=1.0$ reconstructs the
499 hotspot height for the black spruce as same as Maignan method; but a $C_2=8.0^\circ$ can characterize a
500 wider hotspot for matching this measurement in the NIR band. The old back spruce captures a
501 more prominent hotspot signature in the red than in the NIR. For the in-situ data, the fit-RMSEs

502 for the RTLSR, the Maignan and the RTCLSR are 0.0073, 0.0067 and 0.0058 in the red, and
503 0.0530, 0.0515 and 0.0506 in the NIR, respectively. Since these models are consistent in fitting
504 these measurements except for hotspot region, the difference in overall fit-RMSEs results from
505 their hotspot effects.

506  Figure 10 near here

507 **4.4. Sensitivity of hotspot parameters**

508 To examine the sensitivity of hotspot parameters to hotspot-fits, we provide the plots
509 showing the fitting errors (color contour) as functions of C_1 and C_2 at each iteration for the entire
510 POLDER sampled dataset in the red and the NIR bands (Figure 11, top). Results indicate that the
511 C_1 values are more sensitive to hotspot-fit than C_2 , because the fitting errors change more rapidly
512 along C_1 than C_2 . For a given C_2 , fitting errors present certain symmetry about C_1 because large
513 or small C_1 values generate the comparable magnitude of fitting errors. The minimum RMSE
514 occurs at the optimal C_1 and C_2 values (the white point). Similar results were found across IGBP
515 classes.

516 Since the BRDF sampling can have an effect on the sensitivity of model parameter
517 retrievals for kernel-driven models (Lucht et al., 2000), we also examined the sensitivity of the
518 two hotspot parameters to the model parameters. To do this, we evaluated the modeled hotspot
519 reflectance as a function of C_1 (taking $C_2 = 3^\circ$ as the default value) for three sample sizes (i.e., 12,
520 60 and 161 measurements) in principal plane. These BRDF observations are sampled from the
521 airborne CAR cerrado measurements, which contained 29,160 BRDF samples. In each case, 6
522 uniformly-distributed observations in the vicinity of the hotspot region (i.e., $\xi \leq 5^\circ$) were used,

523 and the rest of the observations outside of this hotspot region were randomly sampled.

524 Figure 11 (bottom) presents the sensitivity of modeled hotspot reflectance as a function of
525 C_1 in the red band ($C_2 = 3^\circ$). This figure demonstrates that the BRDF sample sizes have a certain
526 effect on the sensitivity of the C_1 values to the modeled hotspot BRFs, since the hotspot BRFs as
527 a function of C_1 values presents varying slopes for these three cases of BRDF sample sizes. This
528 leads to slightly varying C_1 values, even when using identical hotspot observations for different
529 total BRDF sample numbers. However, the variation range of the modeled BRFs as a function of
530 C_1 can effectively cover the observed hotspot peak (i.e. $HS_{BRF} = 0.23$). Result also indicate that
531 the modeled hotspot BRFs, using the Maignan method, are sensitive to the total BRDF sample
532 numbers in this examination; but with a slight overestimation of the hotspot BRFs. This is
533 consistent with result shown for the NIR band when using MODIS, POLDER and CAR.

534 This investigation demonstrates that the sensitivity of hotspot parameters is somewhat
535 related to varying BRDF sample numbers, which in turn tend to have an effect on model
536 parameter retrievals. This effect holds true even when using the same observations in the vicinity
537 of the hotspot direction (i.e., $\xi \leq 5^\circ$). This implies that the model predicted hotspot BRFs using a
538 set of optimized prior C_1 and C_2 values in RTCLSR model (combining K_{LSR} and K_{RTC}) would
539 be sensitive to the three model parameters (i.e., f_{iso} , f_{geo} and f_{vol}) to a certain extent that the
540 adjustment of hotspot BRF dynamics by three model parameters is no longer effective. In such a
541 situation, the two free hotspot parameters in RTCLSR model provide an improved capacity to
542 capture more accurate hotspot signatures.

543 Figure 10 near here

544 **4.5. Influence on retrieval of intrinsic albedo and clumping index**

545 To evaluate the performance of the RTCLSR method for potential applications, we
546 evaluated the retrieval of intrinsic albedos and clumping index (CI) from available POLDER and
547 MODIS data. The BSA values were calculated for SZAs ranging from 0° to 75° at the interval of
548 15° . In general, the intrinsic albedo retrievals between the RCLSR and RTCLSR models are in a
549 very high correlation for both POLDER ($R^2 = \sim 1.0$) and MODIS ($R^2 > \sim 0.9$) data; with
550 negligible biases ($< \sim 0.0003$ in red and $< \sim 0.0006$ in NIR), while the difference in CI values
551 between models was rather significant (Table 1 and Figure 12). As compared with the RTCLSR
552 model results, a major overestimation of CI values occurs with the RTLSR model, but a slight
553 underestimation of CI values occurs with the Maignan method. This is attributed to the
554 difference in reconstructing hotspot BRFs between models. Figure 12 exhibits the scatter plots
555 between models for $\sim 11,632$ CI values for 15 IGBP classes in the NIR (Figure 12, a-b) and the
556 red bands (Figure 12, c-d) using POLDER data. According to the CI inversion algorithm, the CI
557 biases between models (despite a high correlation, $R^2 = \sim 0.9$) result from biases in modeling
558 hotspot BRFs. For most IGBP classes from POLDER data, about 20% of the relative average
559 difference (RAD) in retrieving CIs occurs between the RTLSR model and the RTCLSR model,
560 while about 10% of RAD occurs between the Maignan method and the RTCLSR in the NIR
561 (Table 1). In the red band (Figure 12, c-d), the RAD in CI retrievals between the Maignan
562 method and the RTCLSR model is generally small, while it still remains about 20% between the
563 RTLSR and the RTCLSR. For the MODIS data, the RAD in CI retrievals arrive at about 6% and
564 12% in the red and the NIR bands between the RTCLSR and the Maignan (Figure 12, e-f).

565 Notably, we use more measurements in CI estimates because we can, in theory, reconstruct the
566 hotspot BRFs using two prior IGBP-based hotspot parameter values that are derived from the
567 high-quality observations in Section 4.1.1. In addition, we merely compare the retrieved CI
568 values between models following the objective of this paper. To extensively validate these CI
569 estimates with ground measurements would require the expanded use of additional
570 measurements beyond the ones used in this study.

571 **5. Conclusions and discussion**

572 In this study, we proposed a new method to correct the hotspot effects for the RTLSR model
573 known for its use within the operational MODIS BRDF/Albedo product. The method makes use
574 of the exponential function with two free parameters (C_1 and C_2) to characterize hotspot height
575 and width. Our results indicate that, although the Maignan method with no free hotspot
576 parameters characterizes the hotspot effect in a relatively high accuracy (particularly for
577 POLDER), the RTCLSR model can provide a further improvement in hotspot-fits. This is mainly
578 attributed to the two free hotspot parameters that can be adjusted to reach their optimal values for
579 the near-hotspot measurements available. Further analysis of the two hotspot parameters using
580 hotspot data reveals that the hotspot signatures are somewhat related to surface type and
581 vegetation phenology for available POLDER data. We found that the hotspot height (C_1) value is
582 bigger in the red band than in the NIR band for most vegetation types, indicating a more
583 prominent hotspot in the red band possibly due to the strong chlorophyll absorption of vegetation
584 foliage.

585 The RTCLSR model is quite consistent with the other two models in the intrinsic albedos

586 retrievals, but is somewhat different in CI retrievals through the use of the inversion algorithm of
587 Chen et al. (2005). This reveals that the albedo retrievals using the RTCLSR would be consistent
588 with the archived albedo product using the routine RTLSR algorithm; however, the RTCLSR
589 model would provide more accurate hotspot signatures that may lead to an improved
590 understanding of vegetation biophysical parameter retrievals in relation to hotspot BRFs. A
591 similar analysis of the RTCLSR with the MODIS hotspot data, airborne CAR data and field
592 measurements reveals the broad adaptability of this new method for different spatial resolutions;
593 however, further investigation into the scale issue of hotspot effect using the RTCLSR model is
594 still a challenge mainly due to the lack of sufficient hotspot data at different spatial resolutions.
595 Investigation into the sensitivity of these two hotspot parameters shows that C_1 is more sensitive
596 to hotspot-fits than C_2 . The total BRDF sampling design can also play a role on the sensitivity of
597 the hotspot parameters to hotspot-fits, because the total sample numbers (even having a good
598 distribution) can have an effect on the model parameter retrievals, in particular the sparse BRDF
599 sampling cases typified by the MODIS retrieval.

600 The original design of the kernel-driven linear Ross-Li BRDF model comprised a collection
601 of kernels for different scenarios of land surface types. Thus, kernel functions are derived from
602 different assumptions for vegetation canopy structures, and view and illumination geometries.
603 These assumptions may result in differences in modeling the radiation field (Wanner et al., 1995)
604 especially in the hotspot direction (Huang & Jiao et al., 2012). Methodologically, the exponential
605 approximation of this hotspot kernel function may also be used to correct the other volumetric
606 scattering kernel (i.e., RossThin), because this exponential hotspot function makes use of two

607 free parameters (C_1 and C_2) to fit hotspot signatures, rather than use surface biophysical
608 parameters as inputs to drive a theoretical hotspot model. The exponential function form is
609 rooted in gap probability theory and has been one of major contributions to hotspot modeling
610 (Qin et al., 1995). The corrected volumetric kernel can be combined with various geometric
611 optical kernels for potential applications. However, the use of multi-kernel combination models
612 would require recalibration of the C_1 and C_2 parameters.

613 In the situation where hotspot signatures are not available, the C_1 and C_2 values would need
614 to be estimated on an *a priori* basis for it to initialize an RTCLSR model inversion. This has been
615 attempted by fitting the hotspot data of several spatial resolutions via two means. Globally
616 optimized C_1 and C_2 values can characterize the overall accuracy of the hotspot effect for certain
617 satellite hotspot data, while variable-related optimized C_1 and C_2 values can help explore hotspot
618 variation as a function of some underlying variables such as surface type and vegetation
619 phenology. We found that a prior $C_1 = 1$ and $C_2 = 3^\circ$ provide a stable initialized value in the
620 RTCLSR model that is comparable in performance to the Maignan method.

621 Because the hotspot effect is very sensitive to the phase angle between the view and
622 illumination in the retro-solar direction (Bréon et al. 2002), its analysis for remote sensing
623 applications requires a very high geometric accuracy. This implies that it is especially difficult to
624 capture accurate hotspot observations in field measurements due to the shadows of the
625 goniometer and sensors that must have a small enough IFOV (e.g., $\leq 1^\circ$). Use of the field
626 measurements with an IFOV = 15° in this study aims to stress that the reciprocal nature allows
627 the RTCLSR model to acquire hotspot-fits with the least RMSEs for this data set. However, with

628 two free hotspot parameters determined *a priori* by using enough hotspot data, this new method
629 provides an improved understanding of the hotspot effect, and thus has potentials for certain
630 ecological applications in regard to the hotspot BRFs for complex heterogeneous environments.
631

632 **6. Appendix A**

633 The shaded area in Figure 1 (a) contains four parts. As the 1st constraint, all observations falling
634 within the phase angle having the radius of R should be included in set **A**. Here, $R = 1.5^\circ$ is used,
635 but R can be adjusted properly for different hotspot data.

$$636 \mathbf{A} = \{ \xi \mid \xi \leq R \}$$

637 To select the observed BRFs close to principal plane (PP) for visually comparing with modeled
638 BRFs in PP, we define the distance, H , which is perpendicular to the principal plane, as the 2nd
639 constraint. Obviously, a less H value can select observations in the shaded area to get closer to PP.
640 This generates set **B** as follows. Here, $H = 10^\circ$ is attempted for MODIS and POLDER data, but H
641 $= 1^\circ$ is attempted for airborne CAR and field data.

$$642 \mathbf{B} = \{ \varphi \mid \theta, \sin \varphi \leq H \}$$

643 As the 3rd constraint, we should consider that, in a 2-D plot that exhibits the observed BRFs in
644 approximate PP, spurious visualizations, particularly in the proximity of hotspot direction in PP,
645 possibly result from some observed BRFs that are not actually near hotspot region in PP, e.g., a
646 $H = 10^\circ$ without other constraints will allow the observed BRFs in the unshaded sector domain
647 taking Sun as the center (Figure 1, a) to be exhibited as near-hotspot BRFs in PP. To remove
648 these observations in 2-D plots that present observed and modeled BRFs in approximately PP
649 (e.g., Figure 1, d), we define an intersection angle (θ) between PP line and the line passing
650 through Sun (Figure 1, a), and derive set **C** and set **D** as follows. Here, $\theta = 45^\circ$ is attempted for
651 these hotspot data used in this study.

$$652 \quad \mathbf{C} = \left(\left\{ \varphi \left| \frac{\sin \theta}{\sin(\pi - \varphi - \theta)} > \frac{\theta_v}{\theta_s} \right. \right\} \cup \{ \varphi \mid \varphi \geq \pi - \theta \} \right) \cap \{ \varphi \mid \theta_v \cos \varphi < \theta_s \}$$

$$653 \quad \mathbf{D} = \left(\left\{ \varphi \left| \frac{\sin \theta}{\sin(\theta - \varphi)} < \frac{\theta_v}{\theta_s} \right. \right\} \cap \{ \varphi \mid \varphi < \theta \} \right) \cap \{ \varphi \mid \theta_v \cos \varphi > \theta_s \}$$

654 Finally, the shaded area in Figure 1 (a) can be derived by implementing set operation for four

655 sets above:

$$656 \quad \mathbf{A} \cup (\mathbf{B} \cap (\mathbf{C} \cup \mathbf{D}))$$

657

658 **7. Acknowledgments**

659 This work was supported by the NSFC (41171261) and the National Basic Research Program
660 (973 Program, 2013CB733400). The POLDER-3/PARASOL BRDFs databases are elaborated by
661 the LSCE, and provided by the POSTEL Service Centre. Many thanks are due to Dr.
662 Francois-Marie Bréon (LSCE, France) for his kindly providing a piece of code to reprocess the
663 POLDER data, and for his great comments and suggestions on this paper.

664

665 Table.

666 Table 1. Statistics of the clumping index values retrieved by three models

Class	Number	RTLRSR		Maignan		RTCLSR		(RTLRSR-RTCLSR)	(Maignan-RTCLSR)
		Mean	Std.	Mean	Std.	Mean	Std.	/RTCLSR (%)	/RTCLSR (%)
ENF	793	0.57	0.04	0.49	0.03	0.51	0.04	13.09	4.32
EBF	898	0.76	0.08	0.56	0.06	0.64	0.07	19.02	11.85
DNF	219	0.66	0.02	0.57	0.02	0.59	0.02	10.54	4.29
DBF	682	0.80	0.06	0.63	0.05	0.67	0.05	19.59	6.89
MiF	690	0.76	0.10	0.57	0.08	0.63	0.09	21.55	9.02
CSh	549	0.77	0.08	0.58	0.06	0.63	0.07	22.83	7.22
OSh	1247	0.86	0.10	0.68	0.10	0.74	0.10	16.31	8.68
Wsa	1035	0.83	0.06	0.62	0.06	0.68	0.06	22.49	8.32
Sav	734	0.87	0.06	0.67	0.06	0.74	0.06	17.64	10.11
GrL	1075	0.88	0.09	0.68	0.10	0.76	0.10	16.21	9.56
Pwe	21	0.95	0.06	0.65	0.05	0.77	0.05	22.29	15.68
CrL	960	0.89	0.07	0.67	0.06	0.75	0.06	19.55	10.48
Ubu	835	0.84	0.06	0.65	0.06	0.72	0.06	17.20	10.13
CNVM	727	0.89	0.06	0.66	0.05	0.75	0.05	19.00	10.94
BSV	1167	0.99	0.16	0.85	0.19	0.92	0.17	8.00	7.44

667

668

669

670 Table 2. The globally optimized C_1 and C_2 values derived from one $10^\circ \times 10^\circ$ tile (h20v11) of MODIS

671 surface reflectance products (MOD09 and MYD09) in 7 reflected solar bands

Band (nm)	Band1 (620-670)	Band2 (841-876)	Band3 (459-479)	Band4 (545-565)	Band5 (1230-1250)	Band6 (1628-1652)	Band7 (2105-2155)
C_1	0.7	0.4	0.7	0.7	0.6	0.7	0.7
C_2 (°)	5.2	4.5	5.2	5.2	3.5	5.2	5.2

672

673

674

675

676 **Figure Captions**

677 Figure 1. (a) The method to select observations near principal plane and in the proximity of hotspot
678 direction to be showed in 2-D plots, its formulation is detailed to appendix A; (b) spatial distribution of
679 view and sun geometries for a typical POLDER data set, i.e., IGBP_01_200609brdf_ndvi08.0824_1671,
680 and (c) for a typical MODIS data set in h20v11 for savanna; (d) the observed and modeled BRFs using
681 Maignan method, and RTCLSR model with $C_1=0.4$, and $C_2=4.5^\circ$ as a function of phase angle for this
682 MODIS data in the NIR. A minus sign is assigned to the phase angle when $\theta_v \cos \varphi < \theta_s$

683 **Figure 2.** LiSparseReciprocal kernel (K_{LSR}) at SZA of 15° , 30° , 45° and 60° (top) and three volumetric
684 kernels in PP (bottom). In the top subplot, the red and magenta dashed curves around the red solid curve
685 are from different h/b and b/r ratios in K_{LSR} . The red solid curve is for the operational K_{LSR} that adopts
686 $h/b=2$ and $b/r=1$; red dashed curve is for $h/b=2$ and $b/r=1.2$; magenta dashed curve is for $h/b=2.5$ and
687 $b/r=1$. In the bottom subplot, three volumetric kernels are for the operational RossThick kernel (K_{RT} ,
688 black curve), the Maignan kernel (K_{RTM} with green solid curve for $\zeta_0 = 1.5^\circ$ and green dashed curve for ζ_0
689 $= 3.0^\circ$), and RossThickChen kernel (K_{RTC}) with $C_1=1$ and $C_2=3^\circ$ (red dashed curve). The upwardly-shifted
690 K_{RTC} with $C_1=1$ and $C_2=3^\circ$ (red solid curve), $C_1=1$ and $C_2=5^\circ$ (blue dashed curve), and $C_1=0.6$ and $C_2=3^\circ$
691 (magenta dashed curve) for a SZA= 30° is aligned with the K_{RT} and K_{RTM} for a convenient comparison.

692 **Figure 3.** The globally optimized C_1 and C_2 values, and the fit-RMSEs derived from the entire POLDER
693 BRDF data in 6 bands (top); the C_1 and C_2 values (middle) and the corresponding fit-RMSEs (bottom) for
694 underlying IGBP class. The dashed lines (top right) present the relative fit-RMSEs (right ordinate)
695 between Maignan method and RTCLSR model. 16 IGBP classes are Evergreen Needleleaf forest (ENF),

696 Evergreen Broadleaf Forest (EBF), Deciduous Needleleaf Forest (DBF), Deciduous Broadleaf Forest
697 (DBF), Mixed Forest (MiF), Closed Shrublands (CSh), Open Shrublands (OSh), Woody Savannas (WSa),
698 Savannas (Sav), Grasslands (GrL), Permanent Wetlands (PWe), Croplands (CrL), Urban and Build-up
699 (UBu), Cropland/Natural Vegetation Mosaic (CNVM), Barren or Sparsely Vegetated (BSV). Snow and
700 Ice (SI) is excluded from this study because of its strong forward scattering.

701 **Figure 4.** Two hotspot parameters (top) as a function of IGBP class in terms of the timing of Jun-Jul-Aug/
702 Dec-Jan-Feb in the northern hemisphere to represent maturity and dormancy season, respectively
703 (opposite in southern hemisphere) in the red and the NIR bands. The corresponding average NDVI and
704 fit-RMSEs (bottom) are presented as a comparison.

705 **Figure 5.** Comparison of the model predicted and observed hotspot BRFs for the entire POLDER BRDF
706 data (upper panel), and two IGBP classes for ENF and WSa (lower panel) in the red band.

707 **Figure 6.** POLDER observations (red points) and the reconstructed BRDF shapes by Maignan (green)
708 and RTCLSR model (black) in 6 bands for the ENF as a function of phase angle in terms of the sampling
709 design (i.e., Figure 1, a)

710 **Figure 7.** Comparison of Maignan with RTCLSR model using CAR/SCAR-B cerrado measurements in
711 principle plane in the red and the NIR bands. We elaborate on the differences between these two models
712 in terms of three cases: (a) and (b) show RTCLSR with the optimal C_1 and C_2 in case 1; (c) and (d) show
713 RTCLSR using $C_1 = 1$ and $C_2 = 3^\circ$ as default values in case 2; (e) and (f) adjust RTCLSR model to
714 approach to Maignan result for deriving the optimal C_1 and C_2 values in case 3.

715 **Figure 8.** Using CAR SCAR-B forests to examine the difference between model predicted and observed
716 BRFs in PP (top) and the difference between RTCLSR and Maignan over the entire viewing hemisphere

717 (bottom) using Flight # 1689 in the red (c) and using Flight # 1693 in the NIR (d).

718 **Figure 9.** Scatterplots showing the difference between modeled and observed BRFs near the hotspot
719 region ($\xi \leq 5^\circ$, red points) and for the viewing hemisphere ($VZA \leq 75^\circ$, black points), using CAR Flight #
720 1689 in the red band (a, b) and CAR Flight # 1693 in the NIR band (c, d)

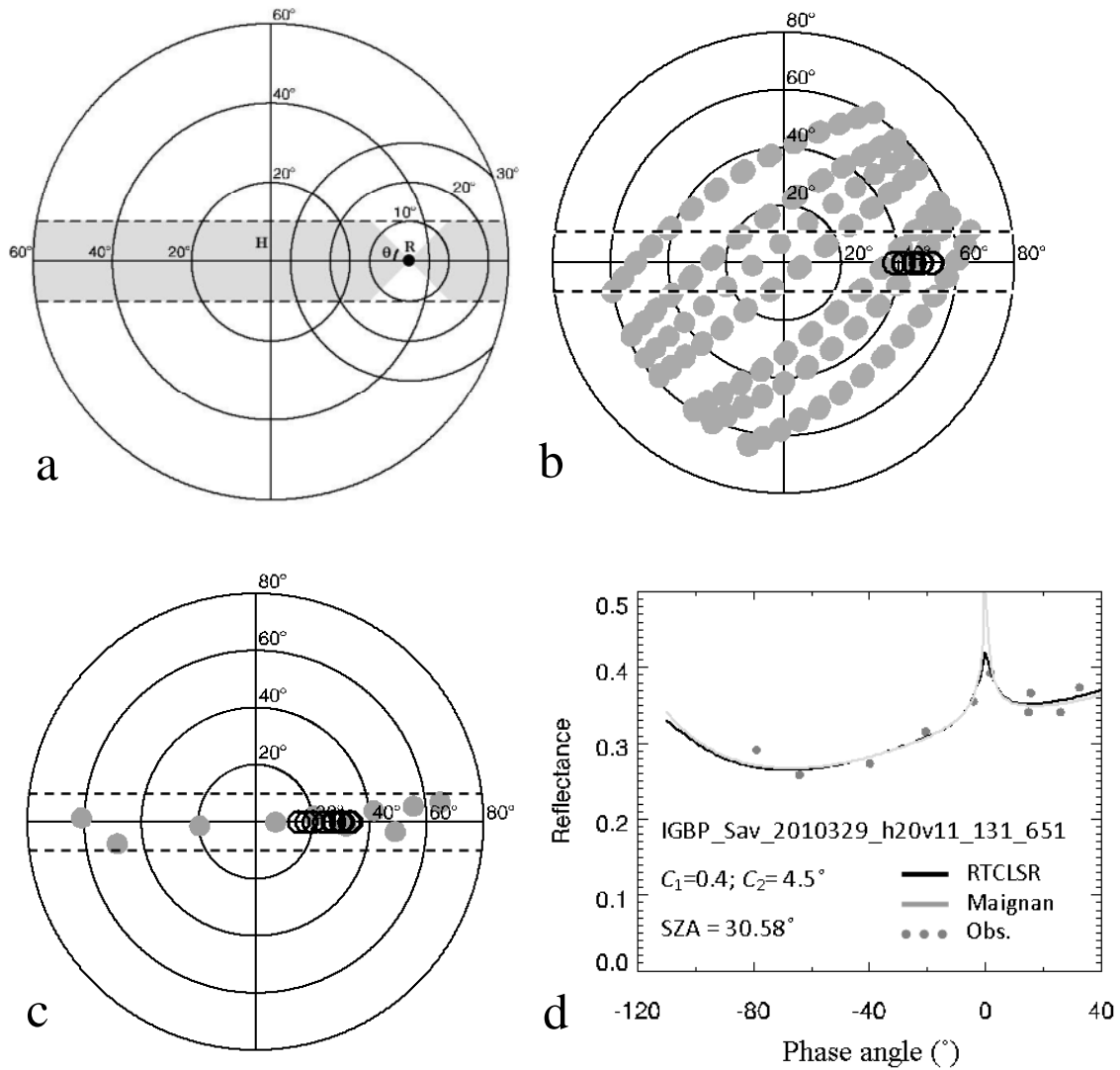
721 **Figure 10.** Comparison of field soil measurements (top) and field old black spruce measurements (bottom)
722 with three models

723 **Figure 11.** The fitting errors as functions of C_1 and C_2 for the entire POLDER data in the red (left) and in
724 the NIR (right), and the white points on the contour plots represent the least fit-RMSEs with the optimal
725 C_1 and C_2 values; the modeled hotspot reflectance as a function of C_1 (given $C_2 = 3^\circ$) using CAR data to
726 simulate three BRDF sample sizes (12, 60 and 161 samples) in the red band (bottom).

727 **Figure 12.** Comparison of CI retrievals between models using POLDER data in the NIR band (top) and in
728 the red band (middle), as well as using MODIS data (bottom) in the red and the in NIR bands. The dashed
729 and solid lines represent the one-to-one lines and the fitted lines, respectively.

730

731

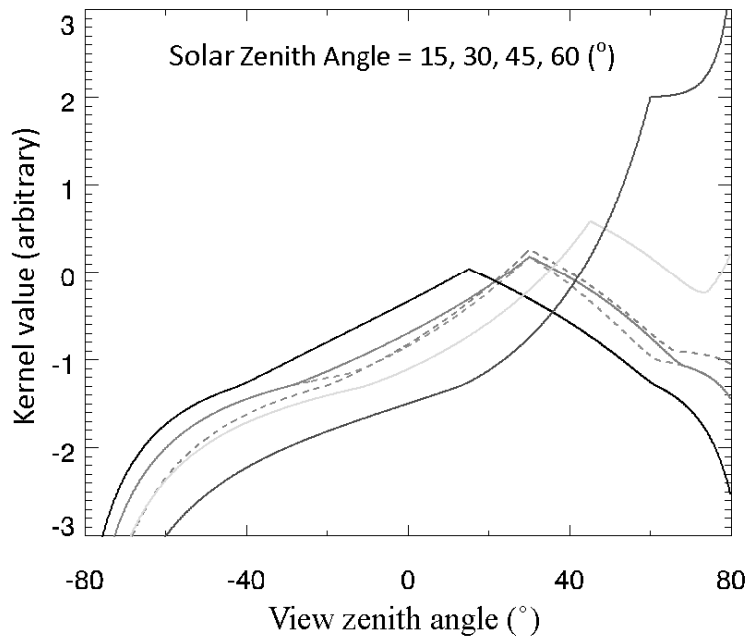


732

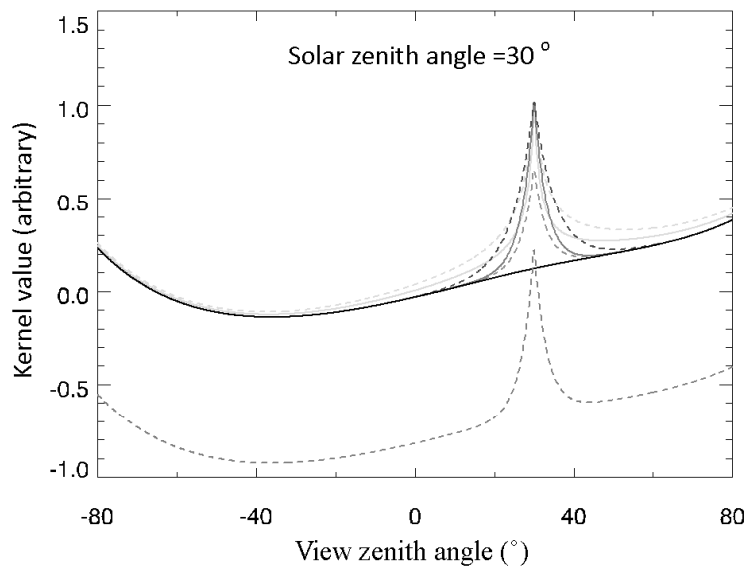
733

734 **Figure 1.** (a) the method to select observations near principal plane and in the proximity of hotspot
 735 direction to be showed in 2-D plots, its formulation is detailed to appendix A; (b) spatial distribution of
 736 view and sun geometries for a typical POLDER data set, i.e., IGBP_01_200609brdf_ndvi08.0824_1671;
 737 (c) for a typical MODIS data set in h20v11 for savanna; (d) the observed and modeled BRFs using
 738 Maignan method, and RTCLSR model with $C_1=0.4$, and $C_2=4.5^\circ$ as a function of phase angle for this
 739 MODIS data in the NIR. A minus sign is assigned to the phase angle when $\theta_v \cos \varphi < \theta_s$

740



741

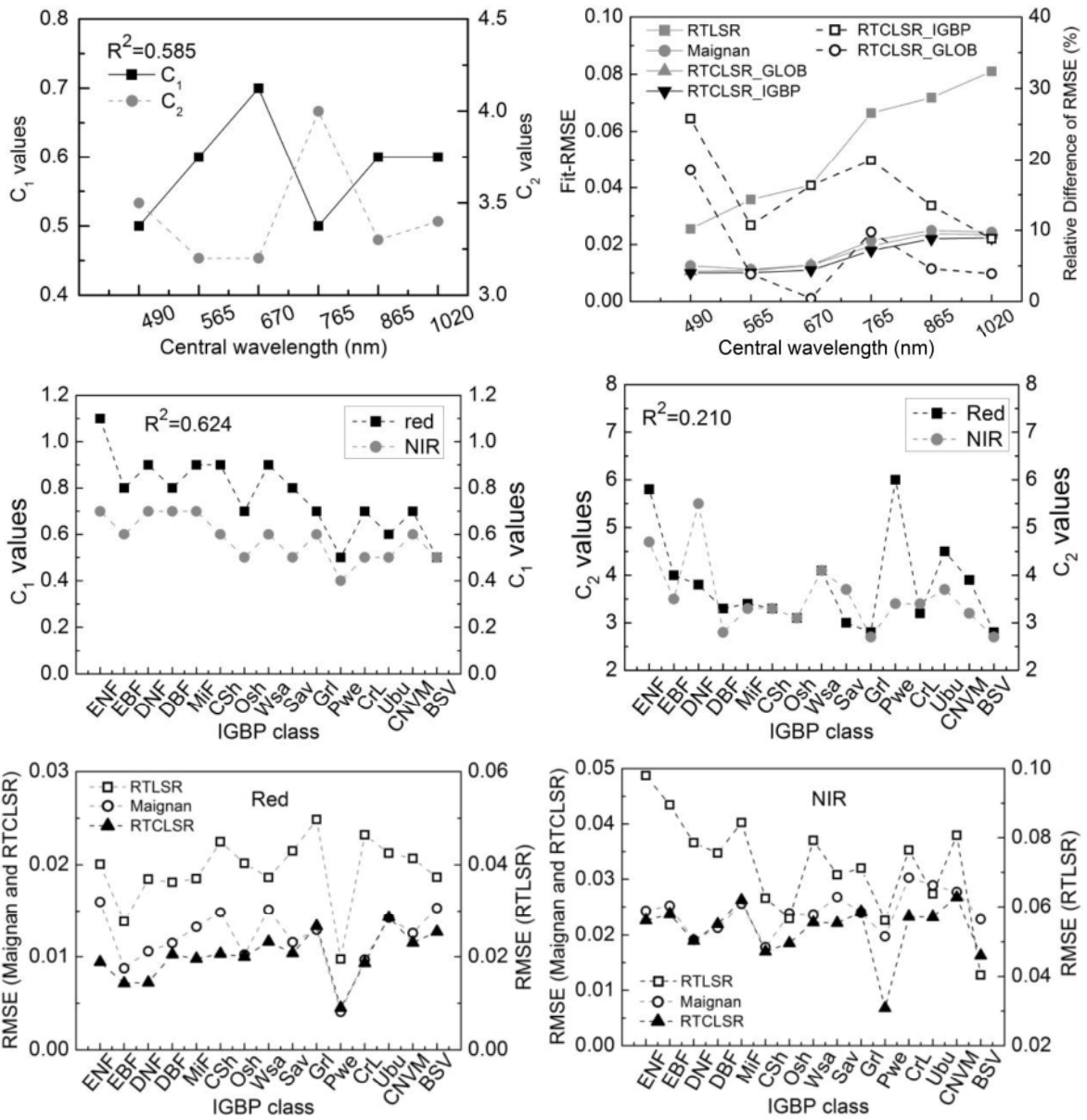


742
743

744 **Figure 2.** LiSparseReciprocal kernel (K_{LSR}) at SZA of 15° , 30° , 45° and 60° (top) and three volumetric

745 kernels in PP (bottom). Details are expounded in figure captions

746



747

748

749

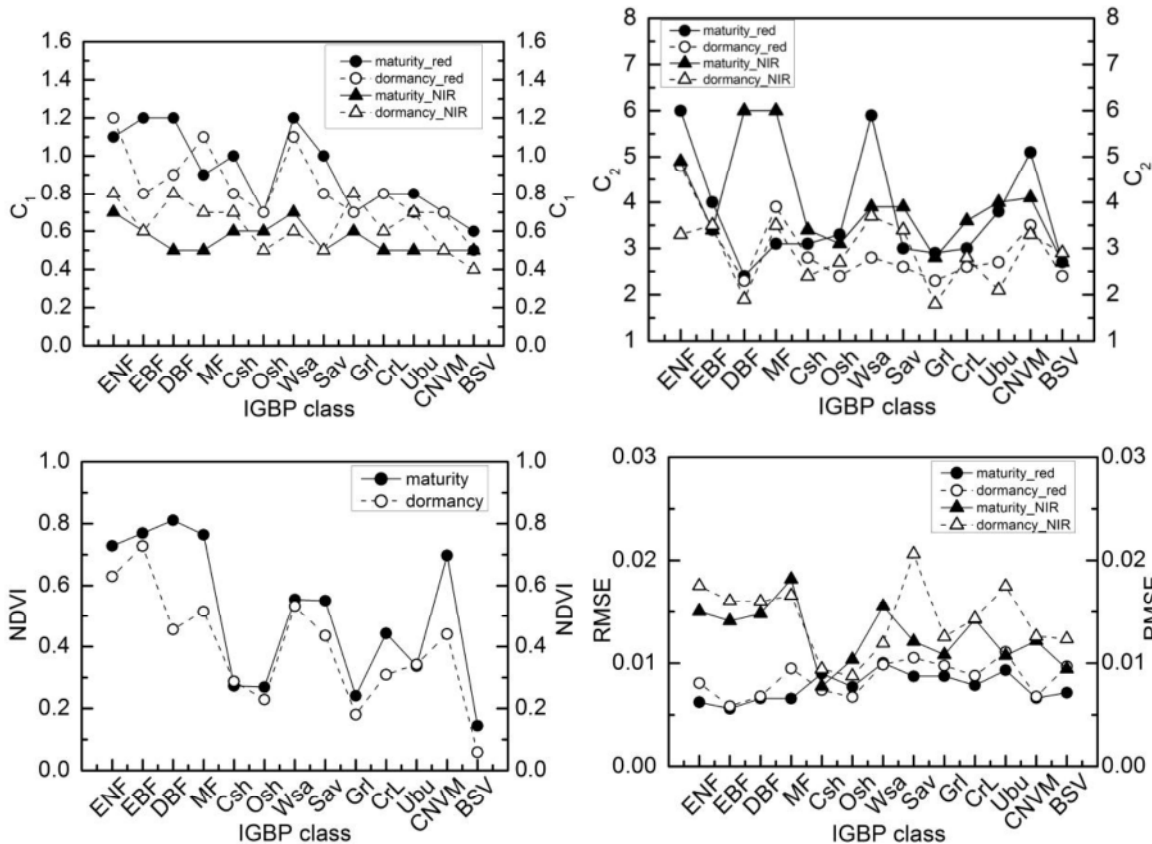
750 **Figure 3.** The globally optimized C_1 and C_2 values, and the fit-RMSEs derived from the entire POLDER

751 BRDF data in 6 bands (top); the C_1 and C_2 values (middle) and the corresponding fit-RMSEs (bottom) for

752 underlying IGBP class. The dashed lines (top right) present the relative fit-RMSEs (right ordinate)

753 between Maignan method and RTCLSR model.

754

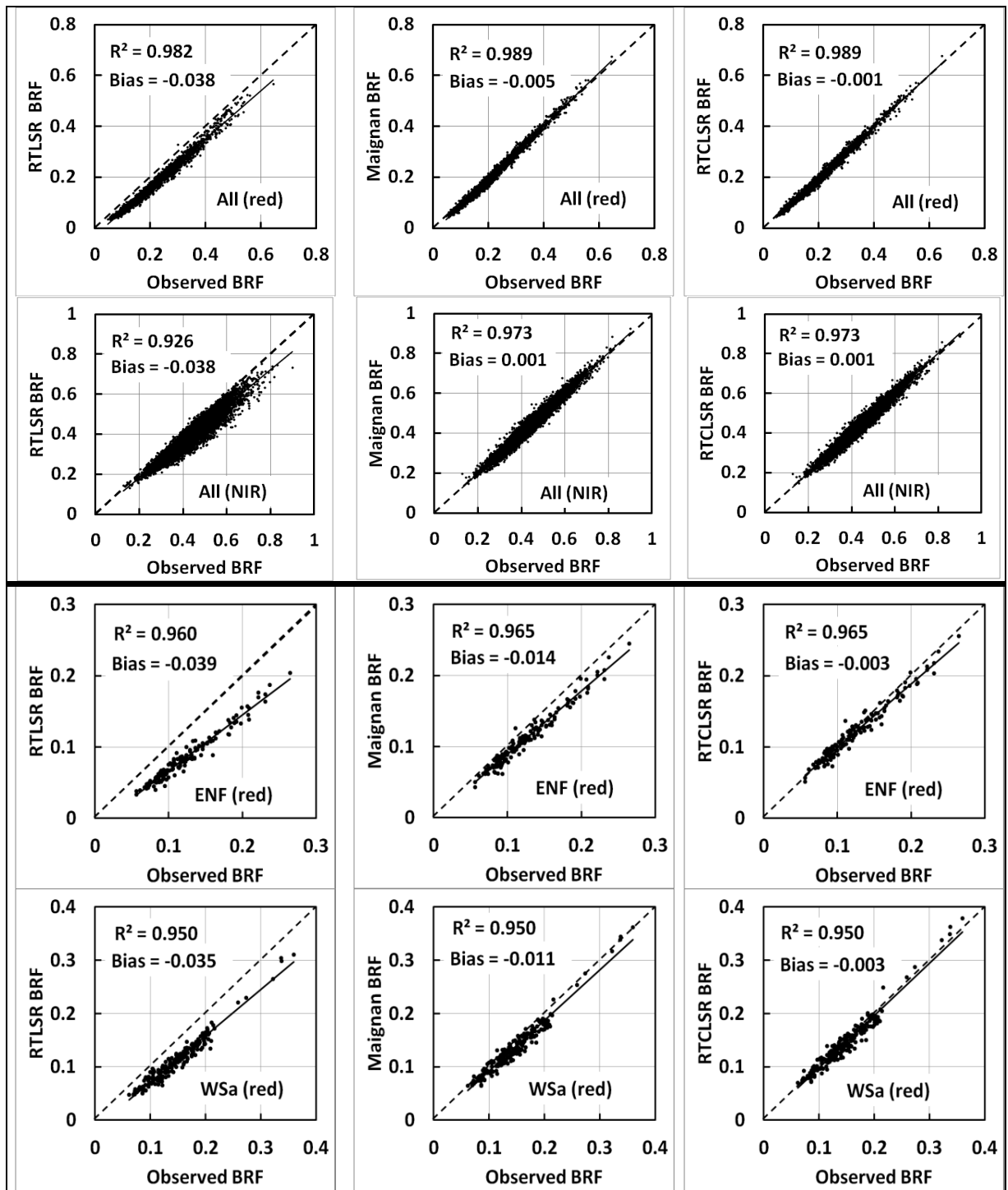


755

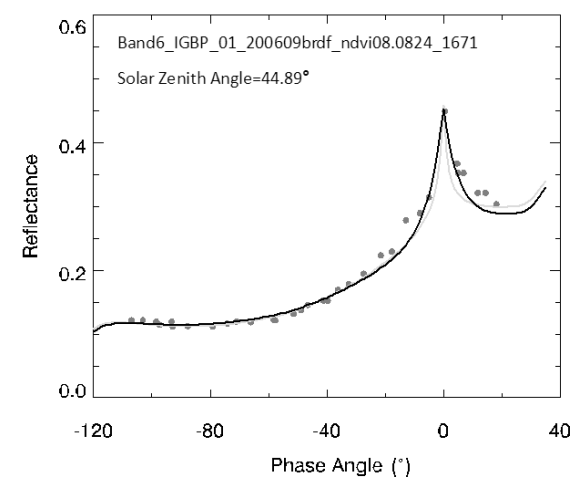
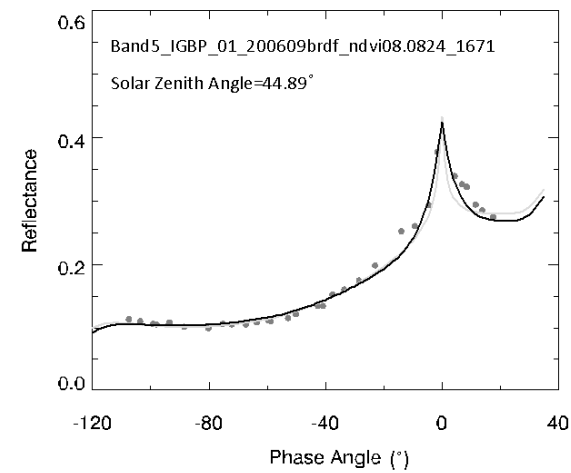
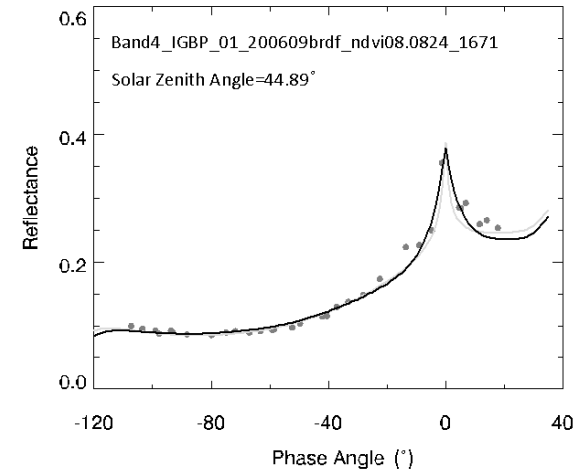
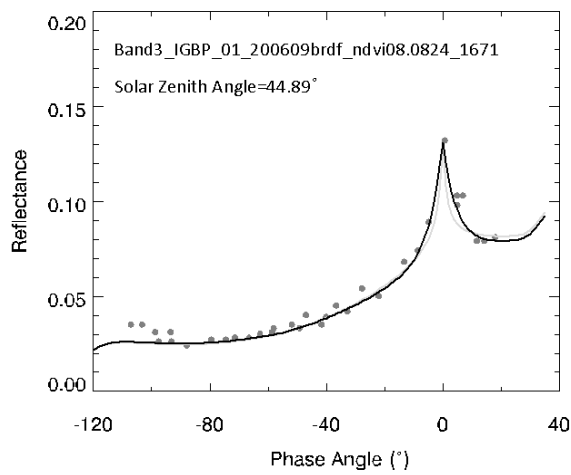
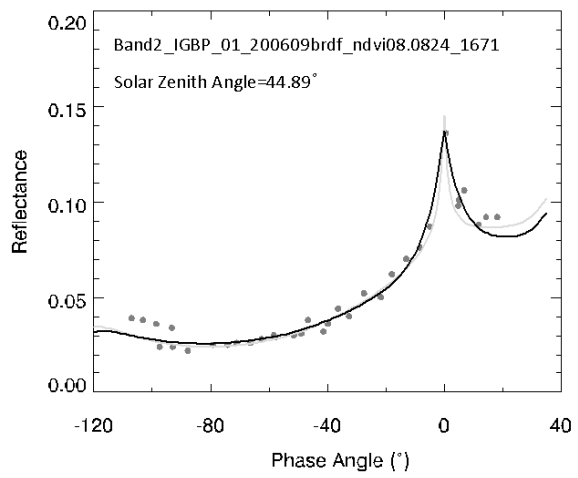
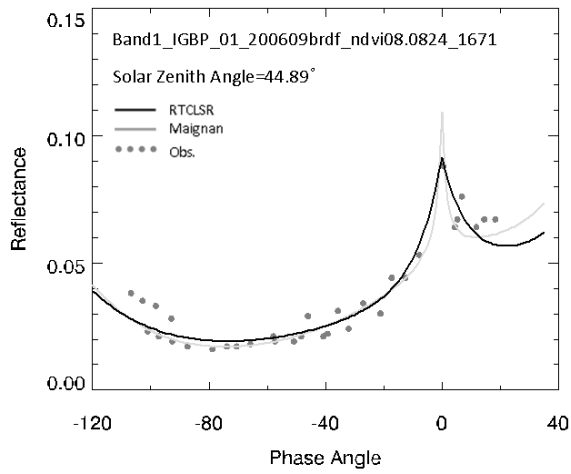
756

757 **Figure 4.** Two hot-spot parameters (top) as a function of IGBP class in terms of the timing of
 758 Jun-Jul-Aug/Dec-Jan-Feb in the northern hemisphere to represent maturity and dormancy season,
 759 respectively (opposite in southern hemisphere) in the red and the NIR bands. The corresponding average
 760 NDVI and fit-RMSEs (bottom) are presented as a comparison.

761



763 **Figure 5.** Comparison of the model predicted and observed BRFs for the entire POLDER BRDF data and
 764 two IGBP classes, i.e., ENF and WSa in the red band.



766

767

768

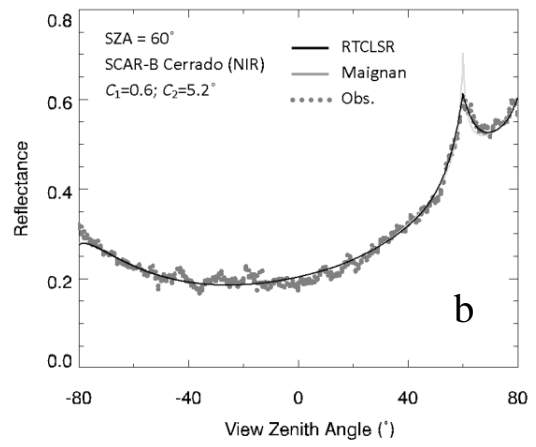
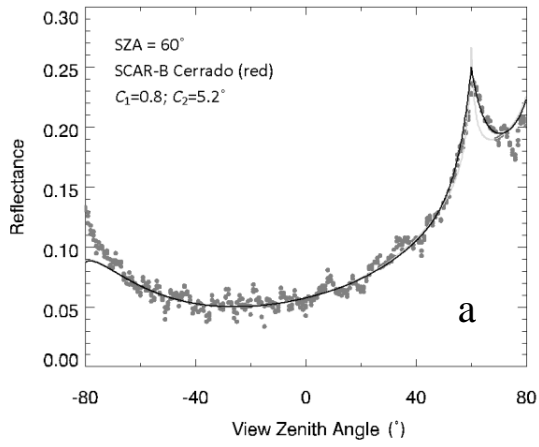
769

770

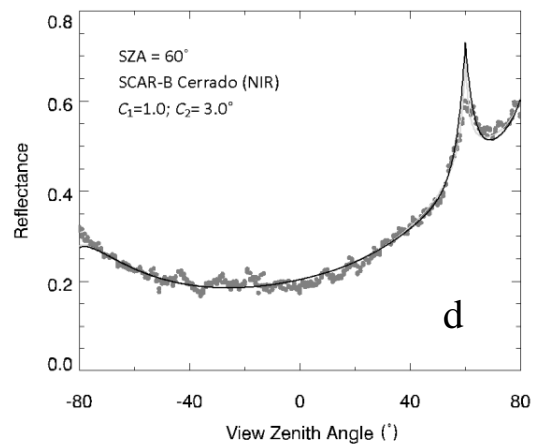
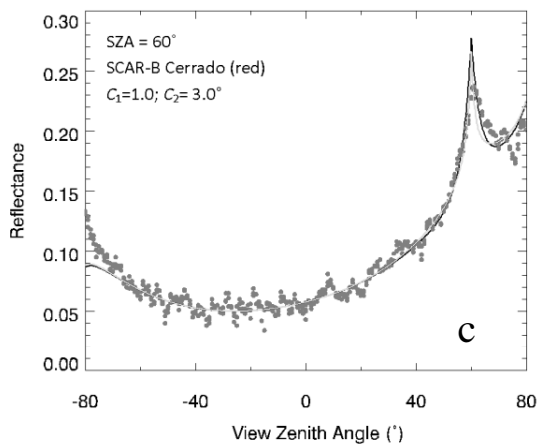
771

772

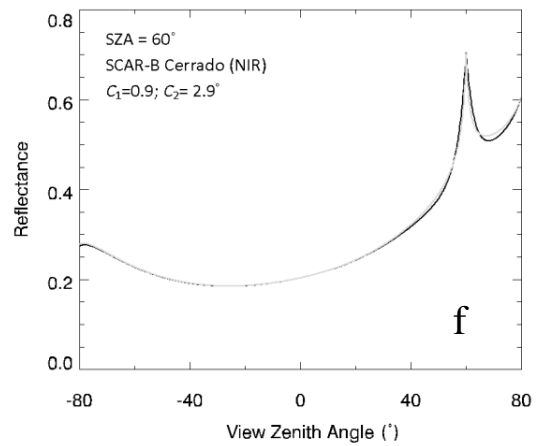
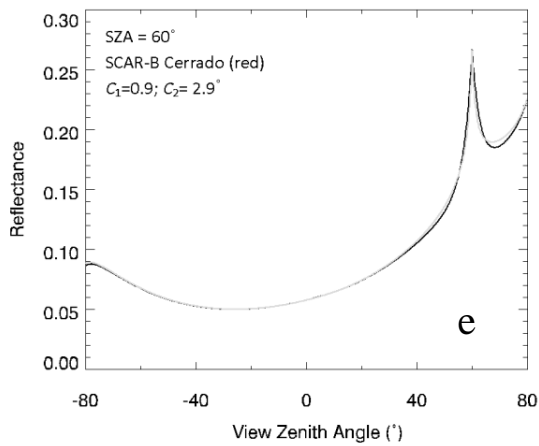
Figure 6. POLDER observations (red points) and the reconstructed BRDF shapes by Maignan (green) and RTCLSR model (black) in 6 bands for the ENF class as a function of phase angle



773



774



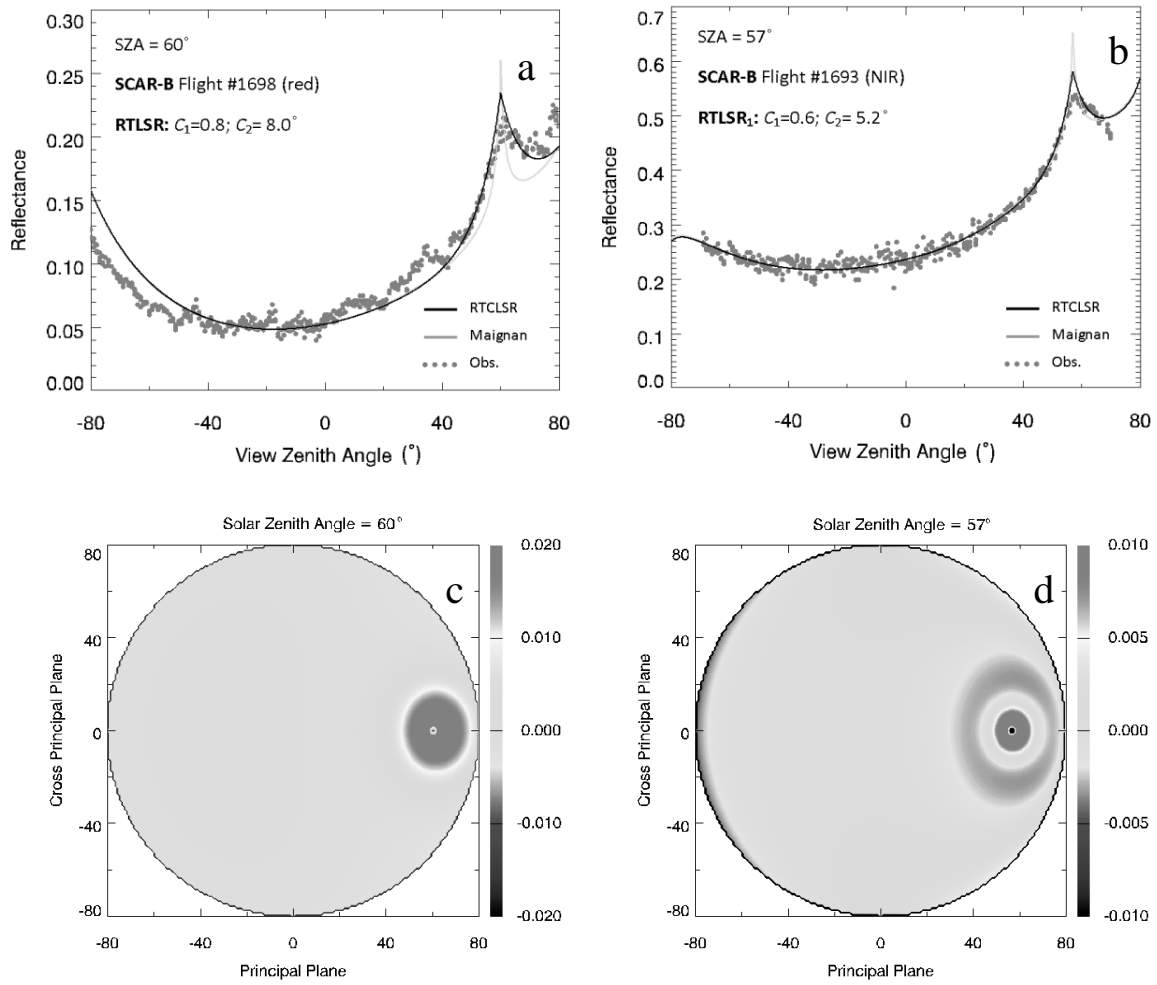
775

776

777 **Figure 7.** Comparison of Maignan with RTCLSR model using CAR/SCAR-B cerrado measurements in

778 principle plane in the red and the NIR bands. Details were expounded in figure captions.

779



780

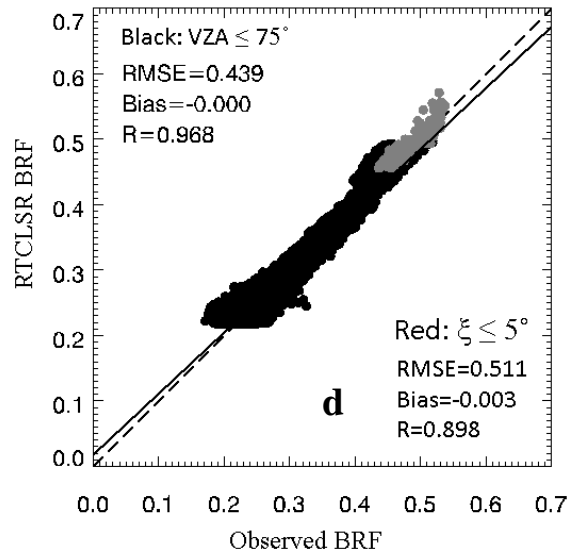
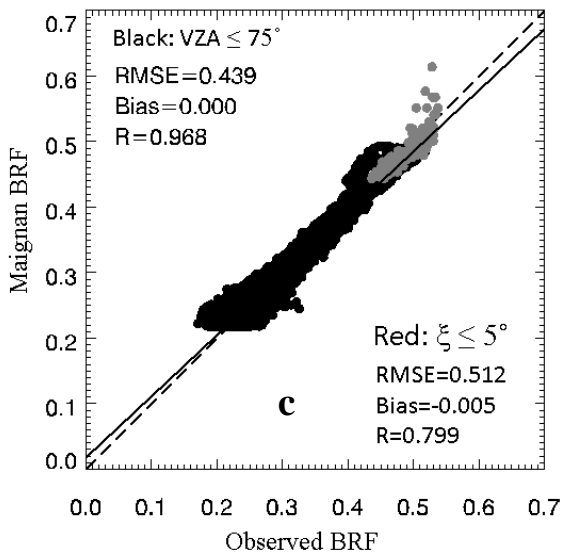
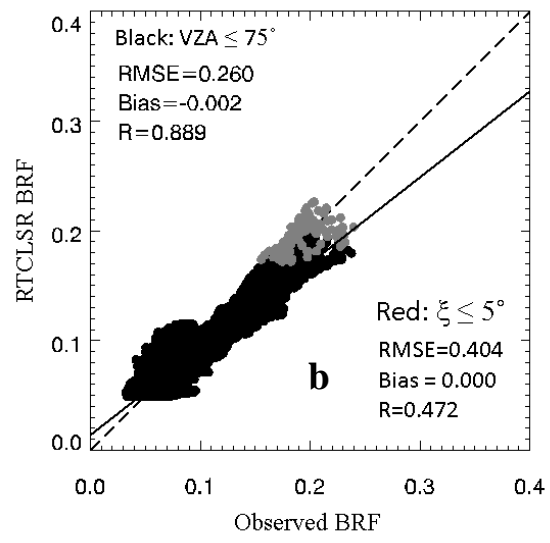
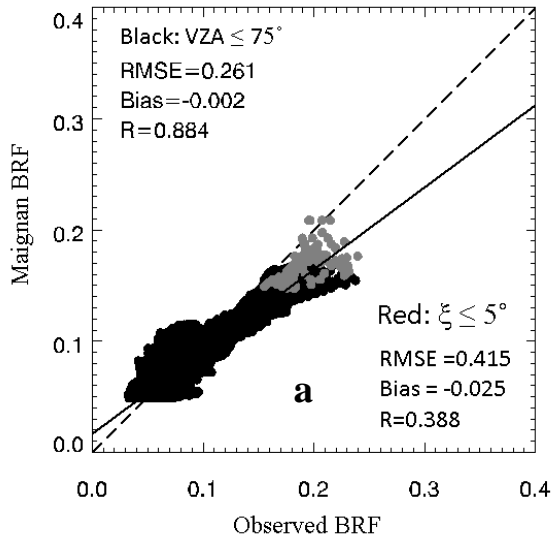
781

782 **Figure 8.** Using CAR SCAR-B forests to examine the difference between model predicted and observed

783 BRFs in PP (top) and the difference between RTCLSR and Maignan over the entire viewing hemisphere

784 (bottom) using Flight # 1689 in the red (c) and using Flight # 1693 in the NIR (d).

785



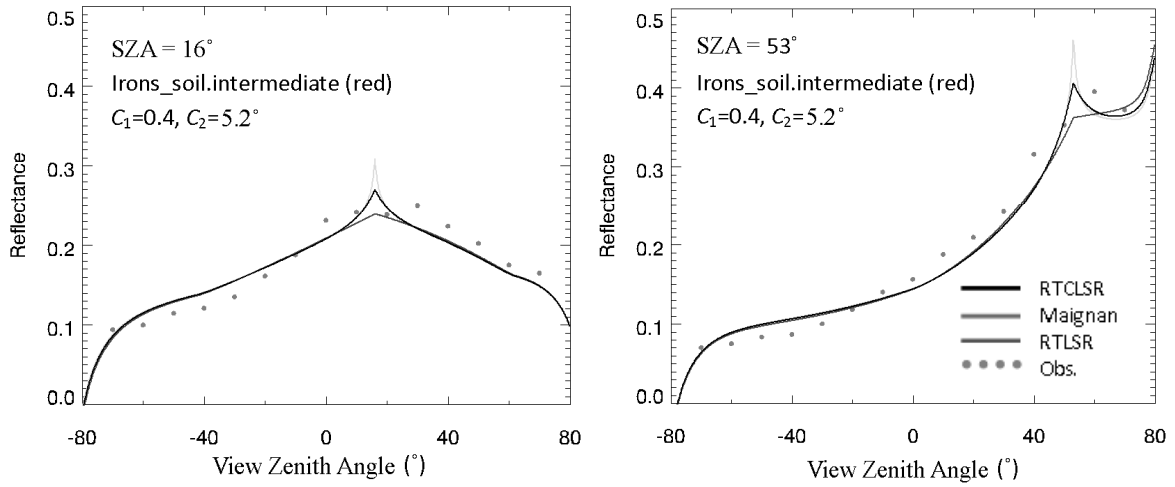
786

787

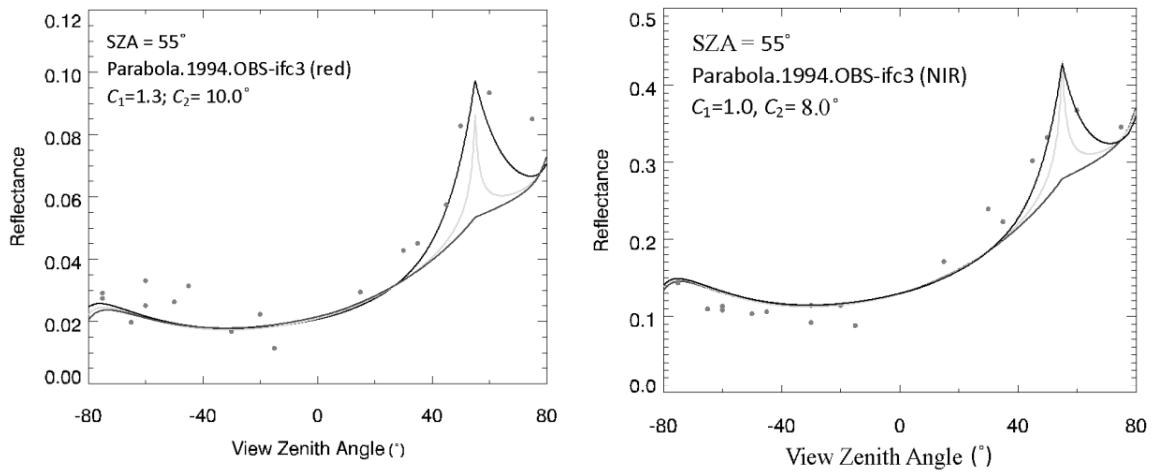
788 **Figure 9.** Scatterplots showing the difference between modeled and observed BRFs near the hotspot
 789 region ($\xi \leq 5^\circ$, red points) and for the viewing hemisphere ($VZA \leq 75^\circ$, black points), using CAR Flight #
 790 1689 in the red band (a, b) and CAR Flight # 1693 in the NIR band (c, d)

791

792



793



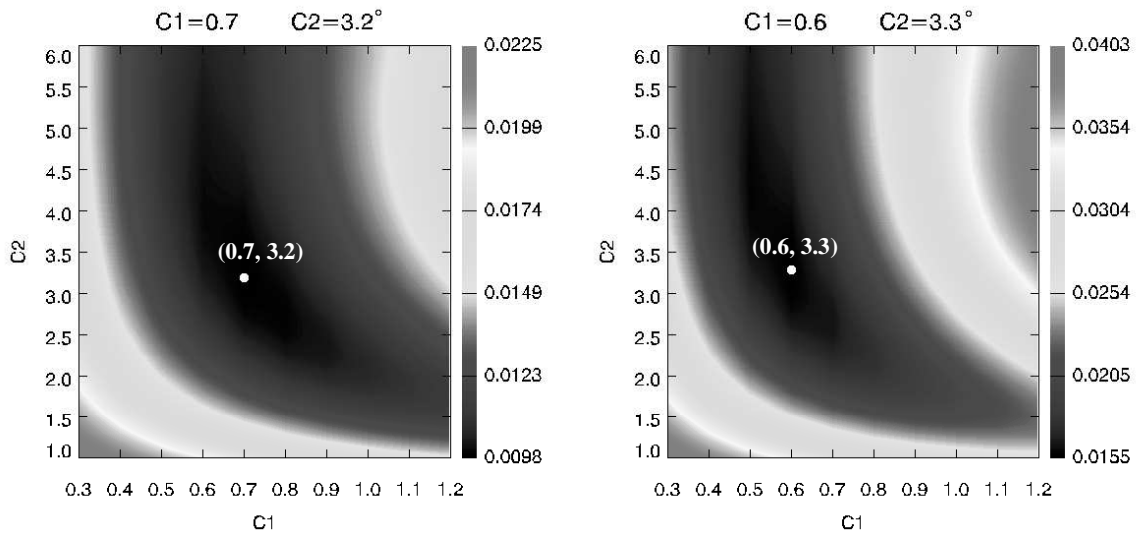
794

795

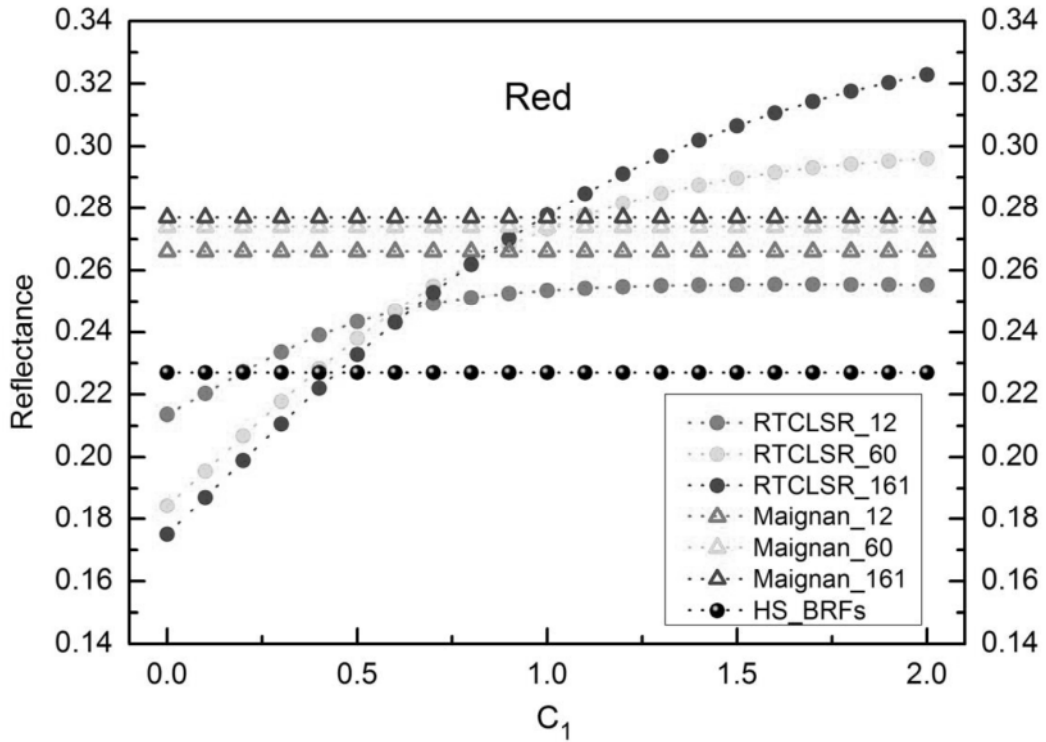
796 **Figure 10.** Comparison of field soil measurements (top) and field old black spruce measurements

797 (bottom) with three models

798



799

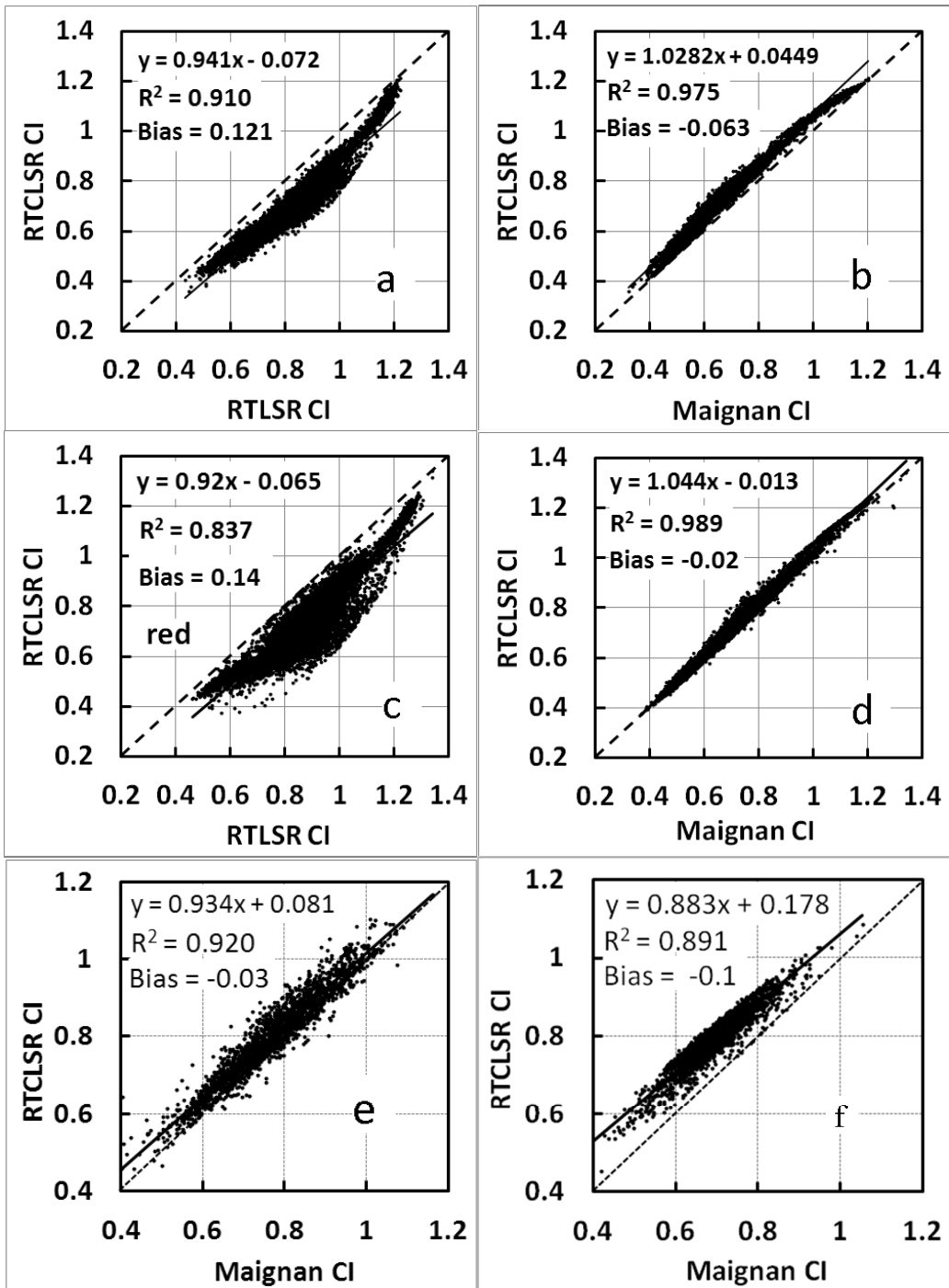


800

801 **Figure 11.** The fitting errors as functions of C_1 and C_2 for the entire POLDER data in the red (left) and in
 802 the NIR (right), and the white points on the contour plots represent the least fit-RMSEs with the optimal
 803 C_1 and C_2 values; the modeled hotspot reflectance as a function of C_1 (given $C_2 = 3^\circ$) using CAR data to
 804 simulate three BRDF sample sizes (12, 60 and 161 samples) in the red band (bottom).

805

806



807

808

809 **Figure 12.** Comparison of CI retrievals between models using POLDER data in the NIR band (top) and in
 810 the red band (middle), as well as using MODIS data (bottom) in the red and the in NIR bands. The dashed
 811 and solid lines represent the one-to-one lines and the fitted lines, respectively.

812

813 **References**

814 Bicheron, P., & Leroy, M. (2000). Bidirectional reflectance distribution function signatures of major
815 biomes observed from space. *J. Geophys. Res.*, *105*, 26669-26681.

816 Bacour, C. and Bréon, F.M. (2005) Variability of land Surface BRDFs. *Remote Sensing Environment*. *98*,
817 80-95.

818 Bréon, F. M., Maignan, F., Leroy, M., & Grant, I. (2002). Analysis of hot spot directional signatures
819 measured from space. *Journal of Geophysical Research* , *107*(16), 4282 – 4296.

820 Bréon, F.M. and the Cnes PARASOL Team, PARASOL Level-1 Product Data Format and User Manual,
821 Issue 1, Revision 1, May, 26th 2005 (www55).

822 Bréon, F. M., Fédèle, E., Maignan, F., & Lacaze, R. (2007). A database of directional reflectance signature
823 (GLC2000) with an analysis tool. *A-Train Symposium. Lille*.

824 Chen, J. M., Rich, P. M., Gower, S. T., Norman, J. M., & Plummer, S. (1997). Leaf area index of boreal
825 forests: Theory, techniques, and measurements. *Journal of Geophysical Research-Atmospheres*, *102*,
826 29429–29443.

827 Chen, J. M., Pavlic, G., Brown, L., Cihlar, J., Leblanc, S. G., White, H. P., et al. (2002). Validation of
828 Canada-wide leaf area index maps using ground measurements and high and moderate resolution
829 satellite imagery. *Remote Sensing of Environment*, *80*, 165 – 184.

830 Chen, J.M., Menges, C.H., & Leblanc, S.G. (2005). Global mapping of foliage clumping index using
831 multi-angular satellite data. *Remote Sensing of Environment*, *97*, 447-457.

832 Chen, J. M., & Leblanc, S. G. (1997). A four-scale bidirectional reflectance model based on canopy
833 architecture. *IEEE Transactions on Geoscience and Remote Sensing*, *35*, 1316–1337.

834 Chen, J. M., & Cihlar, J. (1997). A hotspot function in a simple bidirectional reflectance model for
835 satellite applications. *Journal of Geophysical Research-Atmospheres*, *102* , 25907 – 25913.

836 Chen, J. M., Rich, P. M., Gower, T. S., Norman, J. M., and Plummer, S. (1997), Leaf area index of boreal
837 forests: theory, techniques and measurements. *J. Geophys. Res.* *102*: 29,429–29,443.

838 Chopping, M., Moisen, G.G., Su, L.H., Laliberte, A., Rango, A., Martonchik, J.V., et al. (2008). Large area
839 mapping of southwestern forest crown cover, canopy height, and biomass using the NASA
840 Multiangle Imaging Spectro-Radiometer. *Remote Sensing of Environment*, *112*, 2051-2063.

841 De Colstoun, B.E.C., & Walthall, C.L. (2006). Improving global scale land cover classifications with
842 multi-directional POLDER data and a decision tree classifier. *Remote Sensing of Environment*, *100*,
843 474-485.

844 Deering, D.W., Eck, T.F., & Banerjee, B. (1999). Characterization of the Reflectance Anisotropy of Three
845 Boreal Forest Canopies in Spring–Summer. *Remote Sensing of Environment*, *67*, 205-229.

846 Friedl, M.A., McIver, D.K., Hodges, J.C.F., Zhang, X.Y., Muchoney, D., Strahler, A.H., et al. (2002).
847 Global land cover mapping from MODIS: algorithms and early results. *Remote Sensing of*
848 *Environment*, *83*, 168-182.

849 Friedl, M.A., Sulla-Menashe, D., Tan, B., Schneider, A., Ramankutty, N., Sibley, A., et al. (2010). MODIS
850 Collection 5 global land cover: Algorithm refinements and characterization of new datasets. *Remote*
851 *Sensing of Environment*, 114, 168-182.

852 Geiger, B., Franchistéguy, L., Carrer, D. and Roujean, J.-L. (2005). Land Surface Analysis Satellite
853 Application Facility (LSA-SAF) Product User Manual (PUM) on Albedo. Eumetsat, pp. 41.

854 Gatebe, C. K., King, M. D., Platnick, S., Arnold, G. T., Vermote, E. F., & Schmid, B. (2003). Airborne
855 spectral measurements of surface-atmosphere anisotropy for several surfaces and ecosystems over
856 southern Africa. *Journal of Geophysical Research*, 108 (D13).

857 Gatebe, C.K., Butler, J.J., Cooper, J.W., Kowalewski, M., & King, M.D. (2007). Characterization of
858 errors in the use of integrating-sphere systems in the calibration of scanning radiometers. *Applied*
859 *Optics*, 46, 7640-7651

860 Hautecoeur, O., & Leroy, M. M. (1998). Surface bidirectional reflectance distribution function observed
861 at global scale by POLDER/ADEOS. *Geophysical Research Letters*, 25, 4197 – 4200.

862 Hill, M. J., Román, M. O., Schaaf, C. B., Hutley, L., Brannstrom, C., Etter, A., Hanan, N. P. (2011).
863 Characterizing vegetation cover in global savannas with an annual foliage clumping index derived
864 from the MODIS BRDF product, *Remote Sensing of Environment*, 115 (8): 2008-2024.

865 He, L., Chen, J. M., Pisek, J., Schaaf, C. B., Strahler, A. H. (2012). Global clumping index map derived
866 from the MODIS BRDF product, *Remote Sensing of Environment*, 119, 118-130.

867 Huang, X., Jiao, Z., Dong, Y., Zhang, H., & Li, X. (2013). Analysis of BRDF and Albedo Retrieved by
868 Kernel-Driven Models Using Field Measurements. *IEEE JOURNAL OF SELECTED TOPICS IN*
869 *APPLIED EARTH OBSERVATIONS AND REMOTE SENSING*. 6 (1): 149-161.

870 Irons, J.R., Campbell, G.S., Norman, J.M., Graham, D.W., & Kovalick, W.M. (1992). Prediction and
871 measurement of soil bidirectional reflectance. *Ieee Transactions on Geoscience and Remote Sensing*,
872 30, 249-260.

873 Jiao, Z., Woodcock, C., Schaaf, C.B., Tan, B., Liu, J., Gao, F., et al. (2011). Improving MODIS land cover
874 classification by combining MODIS spectral and angular signatures in a Canadian boreal forest.
875 *Canadian Journal of Remote Sensing*, 37(2), 184-203.

876 Jiao, Z., & Li, X. (2012). Effects of multiple view angles on the classification of forward-modeled
877 MODIS reflectance. *Canadian Journal of Remote Sensing*, 38 (4), 461-474.

878 Jiao, Z., Zhang, H, Li, X. (2012a). To derive a prior database of archetypal BRDF shapes from ground
879 measurements using anisotropic flat index (AFX). Geoscience and Remote Sensing Symposium
880 (IGARSS), 2012 IEEE International. 6753-6756, 22-27 July, Munich, Germany.

881 Jiao, Z., Hill, M., Schaaf, B. C., Zhang, H., Wang, Z., Li, X. (2014). An Anisotropic Flat Index (AFX) to
882 derive BRDF Archetypes from MODIS, *Remote Sensing of Environment*, 141: 168–187.

883 Jiao, Z., Zhang, H., Dong, Y., Liu, Q., Xiao, Q., Li, X. (2015). An algorithm for retrieval of surface albedo
884 from small view-angle airborne observations through the use of BRDF archetypes as prior
885 knowledge. *IEEE JOURNAL OF SELECTED TOPICS IN APPLIED EARTH OBSERVATIONS*

886 AND REMOTE SENSING, DOI: 10.1109/JSTARS.2015.2414925, accepted.

887 Justice, C.O., Román, M.O., Csiszar, I., Vermote, E., Wolfe, R., Hook, S.J., Friedl, M., Wang, Z., Schaaf, C.,
888 Miura, T., Tschudi, M., Riggs, G., Hall, D.K., Lyapustin, A., Devadiga, S., Davidson, C., & Masuoka, E.
889 (2013). Land and Cryosphere Products from Suomi NPP VIIRS: Overview and Status. *Journal of*
890 *Geophysical Research-Atmospheres*, 118, 1-13, doi:10.1002/jgrd.50771

891 Jupp, D. L., and A. H. Strahler, A hot spot model for leaf canopies, *Remote Sens. Environ.* , 38 , 193 – 210,
892 1991.

893 King, M. D., Menzel, W. P., Grant, P. S., Myers, J. S., Arnold, G. T., Platnick, S. E., et al. (1996). Airborne
894 scanning spectrometer for remote sensing of cloud, aerosol, water vapor and surface properties.
895 *Journal of Atmospheric and Oceanic Technology*, 13, 777–794.

896 Kuusk, A. (1991). The hotspot effect in plant canopy reflectance, in Photon-Vegetation Interactions.
897 Applications in Optical Remote Sensing and Plant Ecology (R. B. Myneni and J. Ross, Eds.),
898 Springer-Verlag, Berlin, pp. 139-159.

899 Li, X., Gao F, Wang J D and Strahler A H. (2001). A priori knowledge accumulation and its application to
900 linear BRDF model inversion. *Journal of Geophysics Research*, 106(D11): 11925-11935.

901 Li, X., & Strahler, A.H. (1992). Geometric-optical bidirectional reflectance modeling of the discrete
902 crown vegetation canopy: effect of crown shape and mutual shadowing. *Ieee Transactions on*
903 *Geoscience and Remote Sensing*, 30, 276-292.

904 Li, Z., Cihlar, J., Zheng, X., Moreau, L. and Ly, H. (1996). The bidirectional effects of AVHRR
905 measurements over boreal regions,” *IEEE Trans.Geosci. Remote Sens.*, 34, 1308–1322.

906 Litvinov, P, Hasekamp, O., Cairns, B. (2011). Models for surface reflection of radiance and polarized
907 radiance: Comparison with airborne multi-angle photopolarimetric measurements and implications
908 for modeling top-of-atmosphere measurements. *Remote Sensing of Environment*, 115, 781– 792.

909 Leroy, M., & Roujean, J.L. (1994). Sun and view angle corrections on reflectances derived from
910 NOAA/AVHRR data. *IEEE Transactions on Geoscience and Remote Sensing*, 32, 684-697.

911 Lucht W, Schaaf C B and Strahler A H. 2000. An algorithm for the retrieval of albedo from space using
912 semiempirical BRDF models. *IEEE Transactions on Geoscience and Remote Sensing*, 38(2):
913 977-998 .

914 Maignan, F., Bréon, F.M. and Lacaze, R. (2004). Bidirectional reflectance of Earth targets: evaluation of
915 analytical mode ls using a large set of sp airborne measurements with emphasis with the hot spot,
916 *Remote Sens. Environ.*, 90, 210-220.

917 Qin, W. & Goel, N. (1995). An evaluation of hotspot models for vegetation canopies, *Remote Sensing*
918 *Reviews*, 13 (1-2), 121-159.

919 Qin, W., and Jupp, D.L.B. (1993). An analytical and computationally efficient reflectance model for leaf
920 canopies, *Agric. Meteorol.*, 66, 31-64.

921 Qin, W., and Xiang, Y. (1994). On the Hotspot Effect of Leaf Canopies: Modeling Study and Influence of
922 Leaf Shape. *Remote Sensing of Environment*, 50, 95– 106.

- 923 Roujean, J.-L., Leroy, M., & Deschamps, P.-Y. (1992). A Bidirectional Reflectance Model of the Earth's
924 Surface for the Correction of Remote Sensing Data. *J. Geophys. Res.*, 97, 20455-20468.
- 925 Roujean, J.-L. (2000). A Parametric Hot Spot Model for Optical Remote Sensing Applications. *Remote
926 Sensing of Environment*, 71, 197-206.
- 927 Ross, J.K. (1981). *The Radiation Regime and Architecture of Plant Stands*. Norwell, MA: Dr. W. Junk,
928 392 pp.
- 929 Román, M. O., C. B. Schaaf, P. Lewis, F. Gao, G. P. Anderson, J. L. Privette, A. H. Strahler, C. E.
930 Woodcock, and M. Barnsley (2010), Assessing the coupling between surface albedo derived from
931 MODIS and the fraction of diffuse skylight over spatially-characterized landscapes, *Remote Sensing
932 of Environment*, 114(4), 738-760, doi:10.1016/j.rse.2009.11.014.
- 933 Román, M. O., C. K. Gatebe, C. B. Schaaf, R. Poudyal, Z. Wang, King, M. D. (2011). Variability in
934 surface BRDF at different spatial scales (30 m - 500 m) over a mixed agricultural landscape as
935 retrieved from airborne and satellite spectral measurements, *Remote Sensing of Environment*, 115,
936 2184-2203, 2011.
- 937 Sellers, P. J., Los, S. O., & Tucker, C. J. (1994). A global 1- 1- NDVI data set for climate studies. Part 2:
938 The generation of global fields of terrestrial biophysical parameters from the NDVI. *International
939 Journal of Remote Sensing*, 11, 95–111.
- 940 Schaaf, C.B., Gao, F., Strahler, A.H., Lucht, W., Li, X., Tsang, T., et al. (2002). First operational BRDF,
941 albedo nadir reflectance products from MODIS. *Remote Sensing of Environment*, 83, 135-148.
- 942 Strugnell, N., W. Lucht, and Schaaf, C. (2001). A global albedo data set derived from AVHRR data for use
943 in climate simulations, *Geophys. Res. Lett.*, 28, 191-194.
- 944 Shuai, Y., Schaaf, C.B., Strahler, A.H., Liu, J., & Jiao, Z. (2008). Quality assessment of BRDF/albedo
945 retrievals in MODIS operational system. *Geophysical Research Letters*, 35, L05407
- 946 Tsay, S.C., King, M.D., Arnold, G.T., & Li, J.Y. (1998). Airborne spectral measurements of surface
947 anisotropy during SCAR-B. *Journal of Geophysical Research-Atmospheres*, 103, 31943-31953.
- 948 Van Leeuwen, W. and Roujean, J.-L. (2002). Land surface albedo from the synergistic use of polar (EPS)
949 and geo-stationary (MSG) observing systems an assessment of physical uncertainties, *Remote Sens.
950 Environ.*, 81, no2-3, 273-289, 2002.
- 951 Wang, Z., Schaaf, C.B., Lewis, P., Knyazikhin, Y., Schull, M.A., Strahler, A.H., et al. (2011). Retrieval of
952 canopy height using moderate-resolution imaging spectroradiometer (MODIS) data. *Remote Sensing
953 of Environment*, 115, 1595-1601.
- 954 Wang, Y.,A. Lyapustin, J.L. Privette, R.B. Cook, S.K. SanthanaVannan, E.F.Vermote, Schaaf, C. (2010).
955 Assessment of biases in MODIS surface reflectance due to Lambertian approximation, *Remote
956 Sensing of Environment*, 114,2791-2801.
- 957 Wanner, W., Li, X., & Strahler, A.H. (1995). On the derivation of kernels for kernel-driven models of
958 bidirectional reflectance. *J. Geophys. Res.*, 100, 21077-21089.
- 959 Zhu, G., Ju, W., Chen, J. M., Gong, P., Xing, B. and Zhu, J.(2012). Foliage Clumping Index Over China's

960 Landmass Retrieved From the MODIS BRDF Parameters Product, *IEEE Transactions on*
961 *Geoscience and Remote Sensing*, 50 (6), 2122-2137.
962 Zhang, X., M.A. Friedl, C.B. Schaaf, A. H. Strahler, J.C.F. Hodges, F. Gao, B. C. Reed, and A. Huete
963 (2003). Monitoring vegetation phenology using MODIS, *Remote Sensing of Environment*, 84,
964 471-475.
965